Dynamics of the Wave-Driven Circulation in the Lee of Nearshore Reefs

da Silva, Renan F.; Hansen, Jeff E.; Lowe, Ryan J.; Rijnsdorp, Dirk P.; Buckley, Mark L.

DOI
10.1029/2022JC019013

Publication date
2023

Document Version
Final published version

Published in
Journal of Geophysical Research: Oceans

Citation (APA)
da Silva, R. F., Hansen, J. E., Lowe, R. J., Rijnsdorp, D. P., & Buckley, M. L. (2023). Dynamics of the Wave-Driven Circulation in the Lee of Nearshore Reefs. *Journal of Geophysical Research: Oceans*, *128*(3), Article e2022JC019013. https://doi.org/10.1029/2022JC019013

JGR Oceans

RESEARCH ARTICLE
10.1029/2022JC019013

Dynamics of the Wave-Driven Circulation in the Lee of Nearshore Reefs

Renan F. da Silva[1,2,3,4,5], **Jeff E. Hansen**[1,2,3,5], **Ryan J. Lowe**[1,2,3,4,5], **Dirk P. Rijnsdorp**[6], and **Mark L. Buckley**[7]

[1]School of Earth Sciences, The University of Western Australia, Crawley, WA, Australia, [2]UWA Oceans Institute, The University of Western Australia, Crawley, WA, Australia, [3]Marine Energy Research Australia, The University of Western Australia, Crawley, WA, Australia, [4]ARC Centre of Excellence for Coral Reef Studies, The University of Western Australia, Crawley, WA, Australia, [5]Oceans Graduate School, The University of Western Australia, Crawley, WA, Australia, [6]Environmental Fluid Mechanics Section, Faculty of Civil Engineering and Geosciences, Delft University of Technology, Delft, The Netherlands, [7]U.S. Geological Survey, St. Petersburg Coastal and Marine Science Center, St. Petersburg, FL, USA

Abstract Nearshore rocky reefs with scales of order 10–100 m are common along the world's coastline and often shape wave-driven hydrodynamics and shoreline morphology in their lee. The interaction of waves with these reefs generally results in either two or four-cell mean circulation systems (2CC and 4CC, respectively), with diverging flows behind the reefs and at the shoreline in the 2CC case and flows that diverge in the lee and converge at the shoreline in the 4CC case. By applying a phase-resolving wave-flow model to conduct a detailed analysis of mean momentum balances for waves interacting with nearshore reefs, we develop an understanding of the drivers of 2CC and 4CC flow dynamics and how they vary for different reef geometries and wave and water level conditions. The 2CC or 4CC patterns were primarily driven by alongshore pressure gradients toward the exposed (nonreef fronted) or reef-fronted beach. These alongshore pressure gradients were dependent on the cross-shore setup dynamics governed by the balance between pressure (i.e., related to the setup) and radiation stress gradients, and mean bottom stresses exerted on the water column. If shoreline wave setup in the lee of the reef was less than the exposed beach, a 4CC pattern developed with convergent flow at the shoreline in the lee of the reef; otherwise, a 2CC emerged with divergent flow at the shoreline. Across the parameter space investigated, reef roughness, distance to the shoreline, and beach slope were the three parameters most likely to change the flow patterns between 2CC and 4CC.

Plain Language Summary Small-scale nearshore rocky reefs are found worldwide along a variety of sandy and rocky coastlines. Wave breaking over small reefs drives mean alongshore circulation patterns in their lee that may cause shoreline accretion or erosion. In this study, we apply a wave-flow model to investigate the physical drivers of the mean currents in the lee of small reefs. The alongshore circulation was primarily driven by the differences of the mean water levels between the lee and the adjacent nonreef fronted beaches. Mean water levels increased by wave breaking; however, the onshore-directed mean flows over the reef created offshore-directed bottom stresses that reduced the mean water levels in the reef lee. If the shoreline mean water levels in the lee were less than the adjacent beach, alongshore currents that converged from the adjacent beaches toward the reefs were developed. If the shoreline mean water levels in the lee of the reef exceeded the adjacent beach, alongshore currents that diverged from the reef toward the adjacent beach occurred. The improved understanding of the circulation drivers developed in this study enhances our ability to characterize and predict wave-driven flows in small-scale nearshore reef systems.

Key Points:

- Phase-resolved model simulations were used to understand circulation patterns that occur in the lee of small-scale reefs
- Two-cell and four-cell circulation patterns were primarily driven by alongshore pressure gradients, which depend on the setup dynamics
- A four-cell pattern generally developed if the shoreline wave setup in the lee of the reef was less than the adjacent nonreef fronted beach

Supporting Information:

Supporting Information may be found in the online version of this article.

Correspondence to:

R. F. da Silva,
renan.silva@uwa.edu.au

Citation:

da Silva, R. F., Hansen, J. E., Lowe, R. J., Rijnsdorp, D. P., & Buckley, M. L. (2023). Dynamics of the wave-driven circulation in the lee of nearshore reefs. *Journal of Geophysical Research: Oceans*, *128*, e2022JC019013. https://doi.org/10.1029/2022JC019013

Received 23 JUN 2022
Accepted 1 FEB 2023

Author Contributions:

Conceptualization: Renan F. da Silva, Jeff E. Hansen, Ryan J. Lowe, Dirk P. Rijnsdorp, Mark L. Buckley
Formal analysis: Renan F. da Silva
Funding acquisition: Jeff E. Hansen, Ryan J. Lowe
Investigation: Renan F. da Silva
Methodology: Renan F. da Silva
Software: Renan F. da Silva
Supervision: Jeff E. Hansen, Ryan J. Lowe, Dirk P. Rijnsdorp
Validation: Renan F. da Silva
Visualization: Renan F. da Silva

1. Introduction

Submerged rocky and coral reefs influence the hydrodynamics and coastal processes of many wave-dominated coastlines worldwide. While coral reef systems are typically found at low latitudes, rocky reefs can be found worldwide along a variety of sandy and rocky coastlines (Pondella et al., 2015). For reefs with limited alongshore extent, the alongshore gradients in wave setup (the increase in mean water level due to wave dissipation) result in corresponding alongshore pressure gradients between the lee of the reef and adjacent shorelines not fronted by reefs (hereafter referred to as "exposed" shorelines). These alongshore pressure gradients can be a primary driver of mean alongshore currents in the lee of reefs and can thus influence alongshore sediment fluxes and shoreline changes. Shoreline erosion is typically thought to occur in the lee of reefs (or similar scaled artificial submerged

Writing – original draft: Renan F. da Silva, Jeff E. Hansen, Ryan J. Lowe, Dirk P. Rijnsdorp, Mark L. Buckley
Writing – review & editing: Renan F. da Silva, Jeff E. Hansen, Ryan J. Lowe, Dirk P. Rijnsdorp, Mark L. Buckley

structures) in the case of diverging alongshore currents and sediment transport, whereas converging alongshore currents and sediment transport would promote shoreline accretion (Ranasinghe et al., 2006). A detailed understanding of the dynamics of wave-driven flows in the lee of reefs are thus critical for predicting how the presence of reef structures affect coastal morphodynamics.

While the dynamics of wave-driven flows over reefs have been extensively investigated, most studies have focused on coral reef systems (Lowe et al., 2009; Monismith, 2007), which are typically long and wide (lengths and widths in the order of 1,000 m) (Falter et al., 2013; Quataert et al., 2015). Conversely, smaller scale nearshore rocky reefs have limited alongshore lengths and narrower reef flats (e.g., order of 10–100 m). The hydrodynamics of these smaller reef systems are still not well understood (Segura et al., 2018; Winter et al., 2017), which motivates this study. Unlike fringing coral reefs that extend over large scales (cross-shore dimensions of order of 100–1,000 m, e.g., Buckley et al., 2015) or rocky shore platforms that are attached to the shoreline (Poate et al., 2020), here we focus on small submerged reefs that are detached from the shore, and have geometries that resemble artificial reefs (Black & Mead, 2001) and submerged breakwaters (Dean et al., 1997). Small nearshore rocky reef systems can be found around the world, for example, along the west coast of North America (Pondella et al., 2015), the southeast coast of South America (Duarte Nemes et al., 2019), south of Australia (Segura et al., 2018) and New Zealand (Black & Andrews, 2001).

Several studies have analyzed the mean momentum balances to understand the dynamics of the mean flows and setup in coral reef systems (Buckley et al., 2015; da Silva et al., 2020; Rijnsdorp et al., 2021; Sous et al., 2020). However, for smaller reef systems, existing studies have primarily focused on describing the wave-driven flows (Mulligan et al., 2010) and infragravity wave dynamics (Winter et al., 2017) rather than understanding the flow dynamics as they apply to small reefs generally. For alongshore uniform reefs (e.g., shoreline attached fringing coral reefs), the wave-driven setup tends to be approximately constant shoreward of the reef crest where breaking occurs (Buckley et al., 2015, 2016). Conversely, for reefs with alongshore variability in bathymetry (e.g., small reefs and barrier reefs) water can more readily return to the ocean through onshore flows over shallower portions of a reef that in their lee diverge toward the sides and result in lower setup at the shoreline. Alongshore pressure gradients are driven by the larger setup in the lee of a reef compared to the typically deeper exposed profile, where most waves do not break, or break closer to shore. The net forcing of alongshore pressure and radiation stress gradients together with other momentum terms (e.g., advective accelerations) results in alongshore currents near the shoreline (e.g., Hansen et al., 2015).

The drivers of wave-driven nearshore flows have been studied for diverse coastal morphological features through the analysis of mean momentum balances using laboratory experiments (Haller et al., 2002), field measurements (Apotsos et al., 2008; Feddersen et al., 1998, 2011; Hansen et al., 2014), and numerical modeling (da Silva et al., 2021; Hansen et al., 2013, 2015; Long & Özkan-Haller, 2005; Moulton et al., 2017). Momentum balance analysis using experimental observations or phase-averaged wave models have mostly relied on linear wave theory (LWT) to estimate radiation stresses (e.g., Haller et al., 2002), which may limit their accuracy in describing the drivers of mean flow and setup (particularly for complex reef structures). By intrinsically accounting for the nonlinearities in their governing equations, phase-resolved numerical models are able to represent the range of nonlinear wave motions (e.g., Rijnsdorp et al., 2015; Smit et al., 2014), which makes them suitable to calculate full momentum balances, particularly in the lee of nearshore reefs.

Several studies have applied numerical modeling to reproduce the hydrodynamics over reefs with geometries consistent with existing submerged breakwaters (da Silva et al., 2022; Ranasinghe et al., 2006, 2010). These studies have found that the interaction of waves and reefs drive two-cell or four-cell mean circulation patterns depending on the wave conditions and structure geometries. A two-cell circulation (2CC) pattern is characterized by the presence of diverging currents in their lee extending up to the shoreline (Bellotti, 2004; Haller et al., 2002; Moulton et al., 2017). For a four-cell circulation (4CC) pattern, diverging currents occur at the immediate lee of the reef, but converging currents occur at the shoreline. The circulation patterns 2CC and 4CC have been generally associated with erosive and accretive shorelines, respectively, in the lee of reefs (Ranasinghe et al., 2006). Observations of the beach morphology in the lee of small reefs show that natural sites can oscillate between eroding and accreting shorelines depending on water levels (which influence the reef submergence depth) and wave conditions, with a salient sometimes seasonally occurring in the lee of the reefs (Duarte Nemes et al., 2019; Segura et al., 2018). Given their influence in determining the hydrodynamics and morphologic variability it is important to understand the dynamical linkages between water levels, waves, and flow patterns, particularly given that sea level rise will result in a greater submergence depth of most reefs.

While empirical predictive formulations have been proposed based on numerical simulations to predict whether 2CC or 4CC will occur (i.e., as a function of wave and reef parameters) (da Silva et al., 2022; Ranasinghe et al., 2010), these studies have not investigated the detailed dynamical links between reef and wave parameters to explain the resulting circulation patterns. Existing studies have hypothesized that the difference between 2CC and 4CC relates to the reversal of alongshore pressure gradients (Ranasinghe et al., 2006; Villani et al., 2012), with the alongshore pressure gradients being based on the cross-shore setup profiles over the reef and at the exposed beach. However, a detailed momentum balance analysis is required to understand the role of these pressure gradients relative to other terms in the momentum balance as has been done in other nearshore environments (e.g., Hansen et al., 2015).

Here we study the drivers of the wave-induced flow patterns in the lee of small nearshore reefs, with a focus on explaining the physical mechanisms differentiating 2CC and 4CC circulation patterns observed behind reefs. We apply a phase-resolved wave-flow model to calculate the wave-driven flow over idealized submerged reefs and we consider an extensive parameter space, including a range of wave conditions, water levels, reef geometries, roughness, shapes, and beach slopes (Section 3). Through a detailed momentum balance analysis, we describe the dynamics governing 2CC and 4CC (Section 4.1). Next, we study how the wave, reef, and bed properties influence the overall aspects of the flow patterns (Sections 4.2 and 4.3). Finally, we discuss how our findings help advance knowledge of wave-driven flow dynamics in natural reef systems more broadly (Section 5).

2. Background: Mean Momentum Balances

To investigate the dynamical drivers of the mean circulation behind the reefs, we analyze the mean (wave-averaged) momentum balance. The steady wave-averaged and depth-integrated momentum equation can be written as (e.g., Mei et al., 2005),

$$\overbrace{(d+\eta)U_j\frac{\partial U_i}{\partial x_j}}^{AA} = -\overbrace{g(d+\eta)\frac{\partial \eta}{\partial x_i}}^{PG} - \overbrace{\frac{\partial S_{ij}}{\partial x_j}}^{RSG} + \overbrace{\langle q_B\rangle\frac{\partial d}{\partial x_i}}^{HRB} + \overbrace{\frac{\partial\left\langle\int_{-d}^{\zeta}\tau_{T,ij}\,dz\right\rangle}{\partial x_j}}^{TRSG} - \overbrace{\langle\tau_{B,i}\rangle}^{BS} \tag{1}$$

where x_i and z denote horizontal ($i = 1, 2$ being the Einstein summation convention) and vertical directions, respectively, t is time, the <> indicates time averaging over many wave periods, the subscript B indicates bed, u_i is the horizontal velocity component in i direction, d is the still water depth, ζ is the instantaneous water level deviation from d, η is the mean water level deviation from d, $\tau_{T,ij}$, and τ_B are the turbulent Reynolds stresses and bottom stress, respectively, g is the acceleration due to gravity and q is the nonhydrostatic pressure divided by the seawater density ($q = p - g(\zeta - z)$, where p is the total pressure divided by the density). The velocity signal is decomposed into a mass-flux velocity U_i (Mei et al., 2005):

$$U_i = \left\langle\int_{-d}^{\zeta} u_i\,dz\right\rangle/(d+\eta) \tag{2}$$

and a fluctuating (wave) component $\tilde{u}_i$ ($\tilde{u}_i = u_i - U_i$). The left-hand side of Equation 1 is the advective acceleration ($AA = (d + \langle\zeta\rangle)U_j\partial U_i/\partial x_j$). The right side is composed of a pressure gradient term ($PG = g(d+\eta)\partial\eta/(\partial x_i)$), a radiation stress gradient (wave force) term ($RSG = \partial S_{ij}/\partial x_j$), where the radiation stress S_{ij} is

$$S_{ij} = \left\langle\int_{-d}^{\zeta}\tilde{u}_i\tilde{u}_j\,dz\right\rangle + \left\langle\int_{-d}^{\zeta}p\,dz\right\rangle - 0.5\,g(d+\eta)^2 \tag{3}$$

a term describing the mean hydrodynamic reaction at the bottom ($HRB = \langle q_B\rangle\partial d/\partial x_i$), a turbulent Reynolds stress gradient term ($TRSG = \partial\left\langle\int_{-d}^{\zeta}\tau_{T,ij}\,dz\right\rangle/\partial x_j$), and a bottom stress term ($BS = \langle\tau_{B,iz}\rangle$). Using our terminology, Equation 1 can be rewritten as:

$$AA_i = -PG_i - RSG_i + HRB_i + TRSG_i - BS_i \tag{4}$$

Based on the cross-shore direction convention where positive x is directed offshore from the still water shoreline at $x = 0$ m, a shoreward-directed forcing by radiation stress gradients, pressure gradients and bottom stresses that all contain negative values in their definition in Equation 4, correspond to positive values of RSG_x, PG_x, and BS_x.

3. Methods

3.1. Three-Dimensional Wave-Flow Numerical Model

We applied the nonhydrostatic phase-resolved model SWASH version 6.01 (Zijlema & Stelling, 2005, 2008) to simulate the nearshore hydrodynamics. SWASH is a numerical implementation of the Reynolds Averaged Navier Stokes (RANS) equations,

$$\frac{\partial u_j}{\partial x_j} + \frac{\partial w}{\partial z} = 0 \tag{5}$$

$$\frac{\partial u_i}{\partial t} + \frac{\partial u_i u_j}{\partial x_j} + \frac{\partial u_i w}{\partial z} + \frac{\partial p}{\partial x_i} = \frac{\partial \tau_{T,ij}}{\partial x_j} + \frac{\partial \tau_{iz}}{\partial z} \tag{6}$$

$$\frac{\partial w}{\partial t} + \frac{\partial w u_j}{\partial x_j} + \frac{\partial w w}{\partial z} + \frac{\partial p}{\partial z} = -g + \frac{\partial \tau_{T,zj}}{\partial x_j} + \frac{\partial \tau_{zz}}{\partial z} \tag{7}$$

where w is the vertical velocity. The depth-integration of the continuity equation, Equation 5, results in,

$$\frac{\partial \zeta}{\partial t} + \frac{\partial \int_{-d}^{\zeta} u_j dz}{\partial x_j} = 0 \tag{8}$$

With the multilevel approach, the fluid domain between the bottom $z = -d(x_i)$ and the free surface $z = \zeta(x_i, t)$ is divided into K layers ($k = 1$ and K at the bottom and water surface, respectively), where the governing equations, Equations 5–7, together with the global continuity equation, Equation 8, are resolved. To parameterize the instantaneous bottom stresses τ_B, we used the quadratic friction law,

$$\tau_{B,i} = c_f \left(U_{dep}^2 + V_{dep}^2\right) \frac{u_{B,i}}{\sqrt{u_B^2 + v_B^2}} \tag{9}$$

where c_f is the dimensionless friction coefficient, $U_{dep,i}$ is the horizontal depth-averaged velocity,

$$U_{dep,i} = \frac{\int_{-d}^{\zeta} u_i dz}{d + \zeta} \tag{10}$$

and $u_{B,i}$ is the near-bed horizontal velocity (calculated at $k = 1$). Horizontal turbulent mixing was modeled with a Smagorinsky-type formulation. As we used two vertical layers in the simulations ($K = 2$), which was found to be appropriate to resolve the wave-driven hydrodynamics (see Section 3.3), no additional turbulence closure model was used for vertical mixing.

3.2. Reef Layouts and Parameter Space

We simulated the wave-driven flow across a range of small-scale reefs with geometries consistent with nearshore rocky reefs (Duarte Nemes et al., 2019; Pondella et al., 2015). The reefs were idealized as rectangle-shaped (Figure 1). However, in Section 5.2 other reef shapes with similar crest areas and locations are shown to have overall similar flow patterns. We varied the following reef geometry parameters (see Figure 1 for schematic of the reef, Table 1 for notation, Table 2 for parameter space):

- the distance offshore, measured from the shoreline at $x = 0$ m to the center of the reef crest x_R (subscript $_R$ indicates reef) ($100 \leq x_R \leq 250$ m);

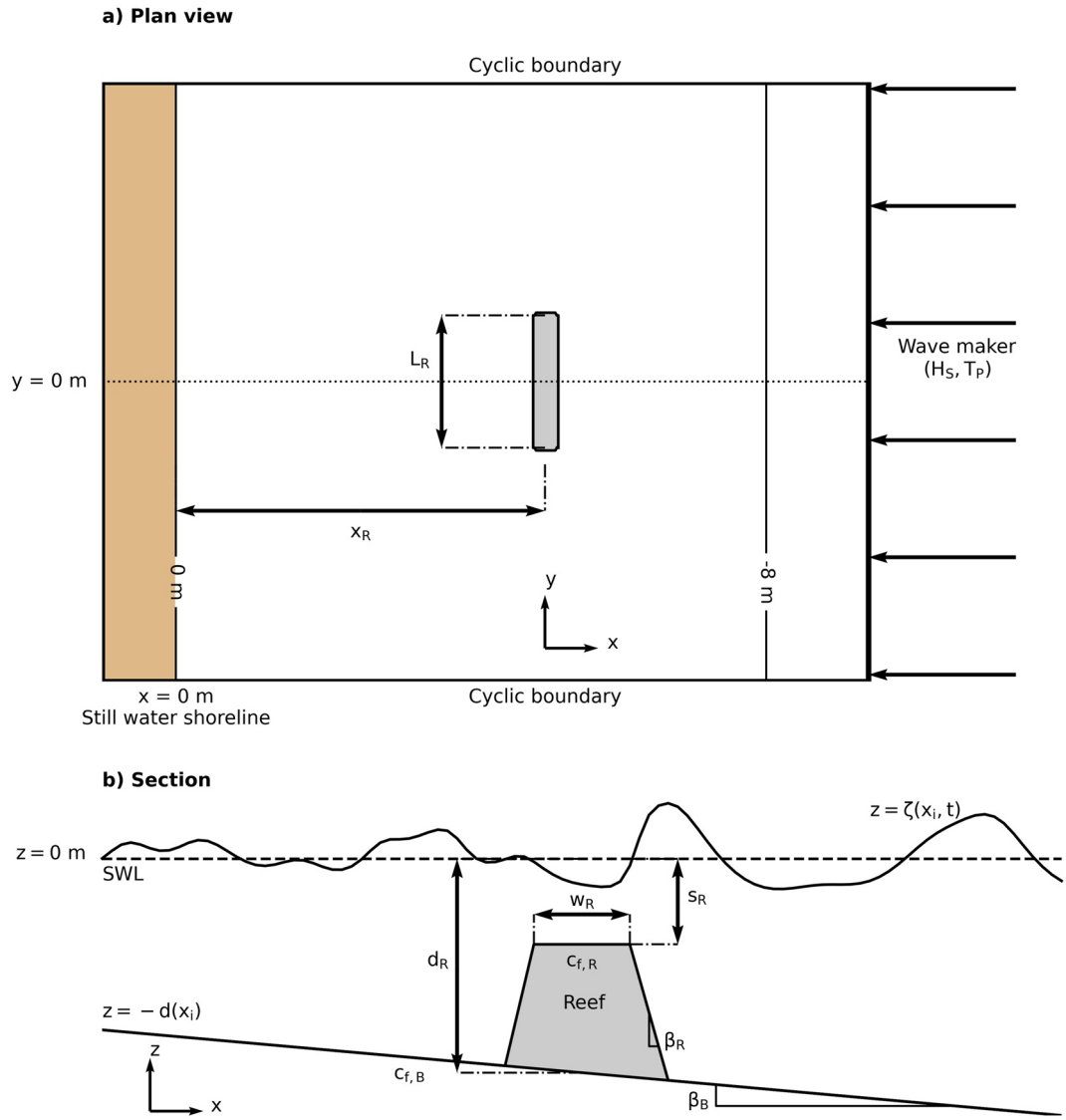

Figure 1. Diagram of the model domain and reef in (a) plan view and (b) cross section with key reef variables labeled.

- the depth d_R of the base of each reef ($2 \leq d_R \leq 12.5$ m);
- the cross-shore crest widths w_R ($10 \leq w_R \leq 50$ m);
- the alongshore crest lengths L_R ($100 \leq L_R \leq 400$ m); and
- the crest level submergence s_R ($-1 \leq s_R \leq -0.5$ m; relative to the still water level (SWL) and negative downward). Note that s_R can also be interpreted as a proxy for the SWL, thus changing s_R could indicate variations of water levels (e.g., tidal fluctuations).

Each reef had a constant 1:1 slope along its perimeter. To investigate the influence of enhanced bottom roughness of the reef relative to adjacent areas, the friction coefficient $c_{f,R}$ of the reefs was varied over the simulations ($0.01 \leq c_{f,R} \leq 0.1$). Note that because we used a phase-resolved model, the c_f relates the instantaneous bottom shear stresses and depth-averaged velocities (Equation 9). Most existing characterizations of friction (or bottom drag) coefficients have focused on those based on mean flow dynamics rather than instantaneous (combined mean and wave orbital currents); thus, we adopted the range of $c_{f,R}$ based on studies of mean momentum balances associated with mean currents observed on reefs (e.g., Rosman & Hench, 2011). In Section 5.1, we briefly discuss implications for uncertainty in $c_{f,R}$ in further detail. The friction coefficient for the surrounding area and beach was kept constant at $c_{f,B} = 0.005$ across simulations, typical for a sandy seabed. The nearshore and beach profile (excluding the reef) had a uniform linear slope $\tan \beta_B$ (i.e., a constant linear slope for the entire shoreface up

Table 1
Notation

Symbol	Definition	Units
c_f	Dimensionless friction coefficient	–
d	Still water depth	m
d_R	Reef base depth (at midcrest) (Figure 1)	m
g	Gravitational acceleration	m s^{-2}
h	Total water depth	m
H_S	Significant wave height	m
$H_{S,0}$	Deep water significant wave height	m
L	Distance between reef center and exposed beach	m
$L_{P,0}$	Deep water peak wavelength	m
$L_{P,wm}$	Peak wavelength at the wave maker	m
L_R	Reef alongshore crest length (Figure 1)	m
p	Total pressure divided by density	m^2 s^{-2}
q	Nonhydrostatic pressure divided by density	m^2 s^{-2}
Q_i	Mass-flux	m^2 s^{-1}
s_R	Reef crest level (Figure 1)	m
T_P	Peak wave period	s
$u_{B,i}$	Bottom-layer horizontal velocity	m s^{-1}
u_i	Instantaneous horizontal velocity	m s^{-1}
$\tilde{u}_i$	Oscillatory horizontal velocity (calculated by subtracting U from u)	m s^{-1}
U_i	Mass-flux velocity	m s^{-1}
$U_{dep,i}$	Instantaneous depth-averaged velocity	m s^{-1}
x	Cross-shore position	m
w	Vertical velocity	m s^{-1}
x_i	Horizontal position	m
x_R	Distance from reef crest center to still water shoreline (Figure 1)	m
w_R	Reef width (Figure 1)	m
y	Alongshore position	m
z	Vertical position	m
β_B	Beach slope (Figure 1)	–
β_R	Reef slope (Figure 1)	–
$\Delta\eta$	Shoreline setup difference between reef center and exposed profile.	m
Δx_i	Grid size	m
ζ	Water level deviation from d	m
η	Mean water level deviation from d	m
η_E	Shoreline setup at the exposed profile	m
η_R	Shoreline setup at the reef center	m
σ_ζ	Water level standard deviation	m
$\tau_{B,i}$	Bottom shear stress divided by density	m^2 s^{-2}

to land, which are hereafter referred to as beach slope). The range of simulated slopes ($0.01 \leq \tan\beta_B \leq 0.05$) spanned mild-sloping ($\tan\beta_B = 0.01$) to steeply sloping ($\tan\beta_B = 0.05$) beach profiles. We note that the variations of reef friction coefficients and beach slopes have not been explored in previous studies (e.g., da Silva et al., 2022; Ranasinghe et al., 2010).

Table 2
Parameter Space

Type	Variable	Notation	Values (reference)	Units
Reef properties	Reef crest submergence	s_R	−1 to −0.5 (−0.5)	m
	Distance from reef crest to shoreline	x_R	100–250 (100[a] and 250[b])	m
	Reef length	L_R	100–400 (200)	m
	Reef width	w_R	10–50 (25)	m
	Reef base depth (at midcrest)	d_R	2–5 (2[a] and 5[b])	m
	Reef friction coefficient	$c_{f,R}$	0.01–0.10 (0.01)	–
Wave parameters	Offshore significant wave height	$H_{S,0}$	0.5–2 (1)	m
	Peak wave period	T_P	5–15 (10)	s
Bed properties	Beach slope	$\tan\beta_B$	0.01–0.05 (0.02)	–

[a]Two-cell circulation (2CC) representative case. [b]Four-cell circulation (4CC) representative case.

To represent common wave conditions found along wave-dominated coastlines, we imposed irregular shore-normal long-crested waves (with one-sided directional spread of 10°) by varying the following wave parameters:

- Offshore significant wave height $H_{S,0}$ ($0.5 \leq H_{S,0} \leq 2$ m); and
- Peak wave periods T_P ($5 \leq T_P \leq 15$ s).

Overall, for this multivariate parameter space we conducted a total of 261 individual simulations. Note that we only considered waves that break over the reefs (roughly indicated by $H_{S,0}/|s_R| > 1$) given their ability to induce stronger nearshore currents (e.g., da Silva et al., 2022).

3.3. Model Setup

The model domain included a single shore-parallel reef superimposed on an otherwise alongshore uniform bathymetry (Figure 1). The wave maker was placed in a flat region with a depth of 8 m, followed by the linearly sloping bed (except at the reef). At the offshore weakly reflective wave maker, we imposed irregular waves with a JONSWAP spectrum including bound waves (Rijnsdorp et al., 2015). At the boundary, shoaling from offshore deep water to the wave maker was accounted for using LWT. At the alongshore boundaries we imposed cyclic conditions, with which the flows recirculate from one side to the other. To minimize boundary effects, the flat region adjacent to the wave maker had a length of 2 times the peak wavelength at the wave maker $L_{P,wm}$, and the distance from the reef to the lateral boundaries was 10 $L_{P,wm}$ (e.g., da Silva et al., 2022). This modeling approach represents the effect of a single reef due to the long distances from the reef to the model lateral boundaries (i.e., limited edge effects, see da Silva et al., 2022).

All simulations had a cross-shore grid resolution Δx of 1.0–1.5 m (with higher resolutions near the beach) and a uniform alongshore grid resolution Δy of 4 m (e.g., da Silva et al., 2022), which resulted in at least 20 cells per peak wavelength at the outer edge of the surf zone. We used two vertically equidistant sigma layers ($K = 2$) that ensured an accurate representation of wave dispersion (Zijlema et al., 2011). Wave breaking was represented with the use of the hydrostatic front approximation (Smit et al., 2013). By using a target Courant number (CFL) of 0.4–0.8 and an initial time step of 0.05 s, SWASH can continuously adjust the time step to ensure model stability.

We adopted a simulation length of 500 T_P. The first 200 T_P served as spin-up before reaching quasi steady hydrodynamic state, and the remaining 300 T_P was used for the model output. For a $T_P = 10$ s, these periods correspond to a simulation length of 1 hr 23 min, with a spin-up time of 33 min and analysis period of 50 min. The spin-up length was calculated by ensuring that the domain-integrated energy and enstrophy reached quasi steady conditions (Feddersen et al., 2011).

3.4. Momentum Balance Analysis

The water level time series were used to calculate the significant wave height $H_S = 4\sigma_\zeta$, where σ_ζ is the water level standard deviation, and the mean water levels η (i.e., the time-averaged difference from SWL), hereafter

referred to as setup. For the mean flow properties, we calculated the mass-flux velocity U_i (Equation 2) and the mean depth-averaged velocity U_{dep} (Equation 10). For simplicity, hereafter we refer to mass-flux velocity U_i as mean currents, whereas specific references to U_{dep} are indicated.

For the momentum balance analysis, we calculated each term in Equation 1 in both the cross-shore (x) and alongshore (y) directions. These momentum terms were calculated according to the method of da Silva et al. (2021), where each term was calculated internally within the model, consistent with SWASH's numerical discretization, ensuring a closure of Equation 1 at computational precision (i.e., effectively no residual errors). As SWASH solves the RANS equations (Section 3.1), we have access to the intrawave (instantaneous) variables (i.e., u_i, ζ, τ_T, τ_B, p, and q) that are needed to calculate each term in Equation 1 as per their definition. As the RANS equations intrinsically compute nonlinear wave motions, the calculation of radiation stresses $S_{i,j}$ considers the nonlinear effects on the oscillatory velocities $\tilde{u}_i$ without the need to rely on often assumed LWT approximations. Given that in this method all mean variables are calculated within SWASH, the mean momentum terms were calculated by considering a sample frequency equal to the inverse of the time step (~20 Hz) without the need to output and store a large amount of data.

3.5. Model Validation

While the overall lack of laboratory or field measurements in similar small rocky reef systems prevents a direct validation of our cases, SWASH has previously been successfully validated in the lee of artificial reef systems (da Silva et al., 2022). Their validation against the wave basin experiments with V-shaped reefs from Ranasinghe et al. (2006) demonstrated the model skills in reproducing the wave-driven flows (note that in this study we use similar reef layout and model setup). In addition, SWASH has been validated in barred beaches with rip channels (da Silva et al., 2021; Villani et al., 2012; Zijlema et al., 2011), whose mean flow patterns (i.e., 2CC and 4CC) are comparable to those observed in reef systems.

4. Dynamics of the Wave-Driven Flows

4.1. Momentum Balances of Representative 2CC and 4CC Patterns

To explain the flow dynamics of 2CC and 4CC patterns, and in particular to understand the dominant drivers of diverging and converging currents along the shoreline, we explored the depth-integrated mean momentum balances for representative 2CC and 4CC cases, shown in Figures 2 and 3, respectively. Using these two examples, we can characterize the overall wave-driven flow patterns resulting from waves breaking on top of reefs. These 2CC and 4CC cases had the same wave conditions ($H_{S,0} = 1$ m, $T_P = 10$ s) imposed over a 1/50 beach slope (Figure 1). For both cases, a reef with width w_R of 25 m, length L_R of 200 m, crest submergence s_R of −0.5 m, and friction coefficient $c_{f,R}$ of 0.01 was considered. The only difference between the representative 2CC and 4CC is the reef distance to the shoreline x_R (which also alters the associated crest base depths d_R), with the reef located at $x_R = 100$ m ($d_R = 2$ m) for the 2CC case and at $x_R = 250$ m ($d_R = 5$ m) for the 4CC case.

4.1.1. Cross-Shore Momentum Balances

For both of the representative cases, waves are attenuated by breaking over the reef (Figures 2a and 3a), which establishes setup gradients (Figures 2b and 3b) and onshore flows across the reef (Figures 2c and 3c). Wave reflection at the reef results in node and antinode patterns of wave heights and setup that are visible offshore of the reef (Figures 2a, 2b, 2d, 2e and Figures 3a, 3b, 3d, 3e). To calculate the reflection coefficient ($H_{S,R}/H_{S,I}$, where the subscripts R and I designate reflected and incident, respectively), we separated the incident and reflected components of the wave with a frequency domain algorithm using LWT (Buckley et al., 2015). The reflection coefficient for the representative cases varied from 0.3 to 0.5 within 100 m offshore of the seaward edge of the reef (not shown). For both cases, the cross-shore flow dynamics over the reef are primarily governed by a balance between shoreward radiation stress gradients (positive RSG_x) resulting from wave breaking (Figures 2d and 3d), and seaward pressure gradients (negative PG_x) associated with the setup (Figures 2e and 3e). The net of these terms is balanced by the advective acceleration AA_x (Figures 2f and 3f) and seaward bottom stresses BS_x (Figures 2g and 3g). Consistent with the variable velocities over the reef, AA_x can be both shoreward and seaward directed and is dominated by $(d + \langle\zeta\rangle)U\frac{\partial U}{\partial x}$ (not shown).

Next, we examined the significance of each of the dominant forcing terms in driving currents (Figure 4). We calculated the magnitude of the dominant forcing terms, the PG, RSG, and AA normalized by their sum. With these normalized magnitudes, the red (AA), green (PG), and blue (RSG) are combined to form colors, whose

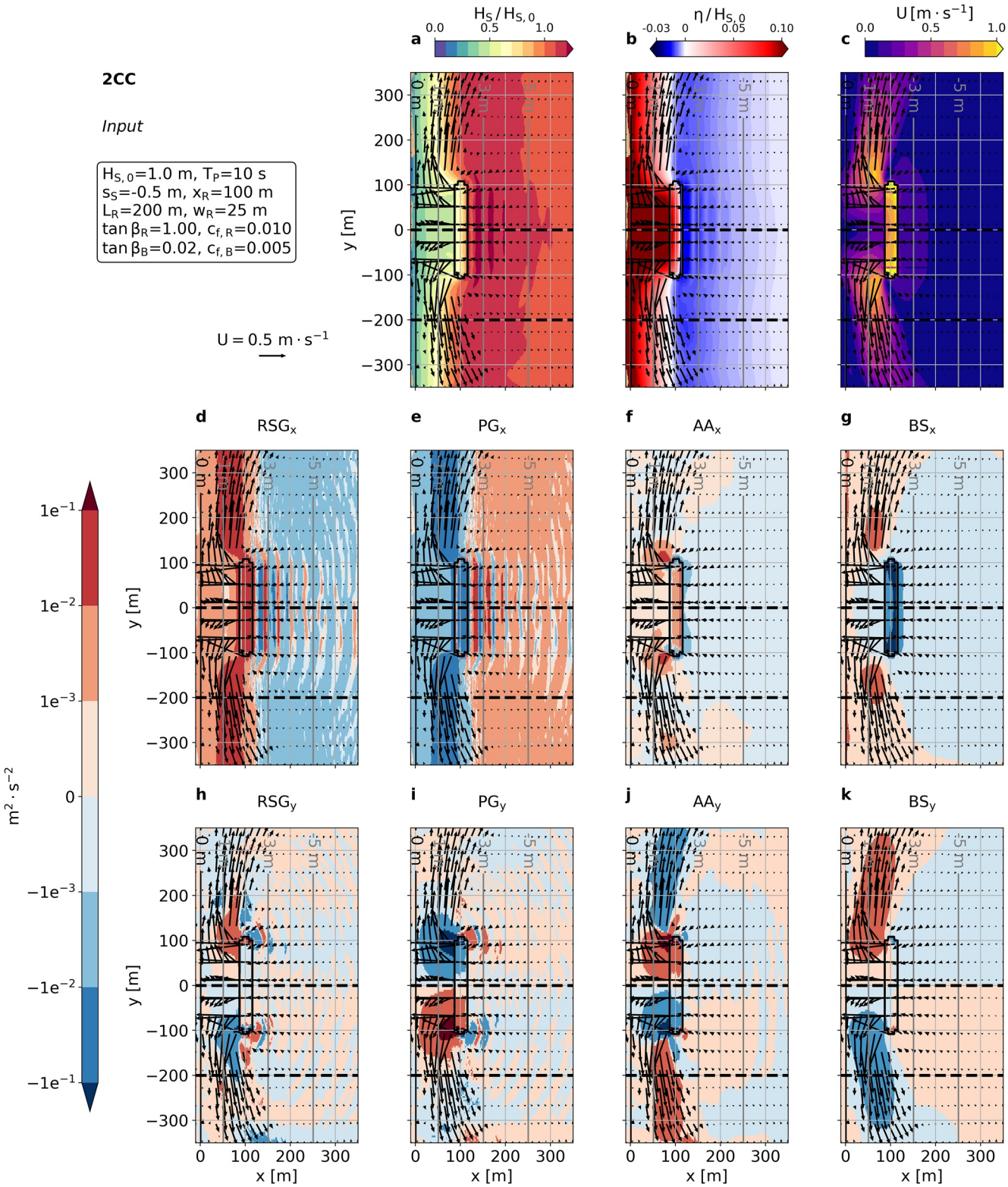

Figure 2.

spatial variations inform where each term (or their combination) dominates. In regions with the basic colors (red, green, and blue), a single momentum term dominates and is counteracted by BS, whereas in regions with no currents (thus with zero BS), the combination of terms driving the balance equals zero. We included numbered markers in Figure 4 to represent places with well-established momentum regimes. The overall dominance of the PG_x and RSG_x is observed both offshore and onshore of the reef (markers 1 and 2, respectively, in Figures 4a and 4c). For the 4CC case, parts of the lee of the reef are partially dominated by AA_x (e.g., marker three in Figure 4c), which occurs where the cross-shore currents reverse from onshore to offshore.

4.1.1.1. Cross-Shore Profiles Over Reef Center and Exposed Profile

The cross-shore profiles over the reef center ($y = 0$ m) and at the exposed profile (calculated at $y = -L_R/2 - x_R$, where alongshore currents near the shoreline are limited—see dashed lines in Figures 2 and 3) indicate that waves rapidly break over the reef (Figure 5a) and drive an increase in the setup in the immediate lee of the reef (Figure 5b). This is in contrast to the more mild wave breaking and gradual increase in setup across the exposed profile (Figures 5a and 5b). At the center of the reef ($y = 0$ m), the flow accelerates over the seaward reef slope and decelerates over the shoreward slope (Figures 2f and 3f). While their cross-shore balances are qualitatively similar, the 2CC case is characterized by weaker onshore flow and larger setup than the 4CC case for the same wave forcing (Figures 5a and 5c).

To understand the mechanisms responsible for the different cross-shore setup profiles between the 2CC and 4CC cases, we investigated the role of different momentum terms in driving setup. With the physical mechanisms driving the setup dynamics for 2CC and 4CC cases, we can estimate the alongshore pressure gradients that largely influence the alongshore flow dynamics (Section 4.1.2). According to Equation 1, the cross-shore pressure gradient PG_x is balanced by all remaining cross-shore momentum terms and thus allows us to reconstruct the setup using different combinations of cross-shore momentum terms. By comparing the reconstructed and modeled setup, we assessed the relative importance of each term in driving setup. With a zero setup offshore as a boundary condition, the reconstructed setup was calculated iteratively from the offshore boundary shoreward. We analyzed the setup profile at the reef center ($y = 0$ m) and exposed beach ($y = -L_R/2 - x_R$) for the representative 2CC and 4CC cases.

The setup reconstruction using only the RSG_x term (denoted $\eta^{recon}_{RSG_x}$) results in increased setup in the reef lee extending up to the shoreline for both cases (Figure 5b). The setup profile reconstructed with both RSG_x and BS_x terms ($\eta^{recon}_{RSG_x+BF_x}$) reduces the bias and approaches the actual model predicted setup (Figure 5b), consistent with the dominance of these terms (along with PG_x) in the cross-shore momentum balance. Due to the seaward mean bottom stresses (Figure 5d) that arise in response to onshore flows U_{dep} (Figure 5c), the reef roughness acts as a sink of momentum and reduces the setup. In contrast to over the reef, the setup at the exposed profile can be accurately reconstructed with only RSG_x ($\eta^{recon}_{RSG_x}$; Figure 5b) that characterizes a classic balance between RSG_x and PG_x (Longuet-Higgins & Stewart, 1964). Unlike the reef profile, a shoreward-directed BS_x develops in response to the undertow approaching the shoreline ($x < 10$ m, Figures 5c and 5d); however, the setup contribution from the BS_x term is negligible (note that in Figure 5b the black dashed and dotted lines coincide). The shoreline setup is larger for 2CC than for 4CC cases (Figure 5b) because of the more efficient momentum transfer from RSG_x to PG_x (under similar offshore wave forcing) combined with the lower setup reduction due to weaker U_{dep} and BS_x for the 2CC (Figures 5c and 5d). As a result, the setup at the exposed profile exceeds the 4CC reef setup at $x = 80$ m and the larger setup near the shoreline results in alongshore pressure gradients and converging flows, which do not occur for the 2CC (Figure 5b).

4.1.2. Alongshore Momentum Balances

For the 2CC case, in the reef lee and near the shoreline ($0 < x < 80$ m), the wave heights are lower and the setup larger than at the exposed profile (Figures 5a and 5b). As a consequence, when considering the alongshore

Figure 2. Plan views of (a) normalized significant wave height $H_S/H_{S,0}$, (b) normalized setup $\eta/H_{S,0}$, (c) mass-flux velocity magnitude U, and (d–k) depth-integrated mean momentum terms for a representative case of two-cell circulation (2CC) resulting from waves interacting with reefs. In all panels, vectors indicate the mass-flux velocities U_i whereas colors indicate each variable. (d, h) Radiation stress gradient RSG in the x-(d) and y-(h) directions. (e, i) Pressure gradients PG in the x-(e) and y-(i) directions. (f, j) Advective acceleration AA in the x-(f) and y-(j) directions. (g, k) Bottom stress BS in the x-(g) and y-(k) directions. The definition of each momentum term is given in Equation 1 and we note that the remaining terms had negligible contributions. The gray and black lines give the depth and reef contours, respectively. The dashed black lines give the reef center and exposed beach transects (see Section 4.1). The simulation input conditions are listed on the upper left table (see Figure 1 and Table 1 for definition of each variable).

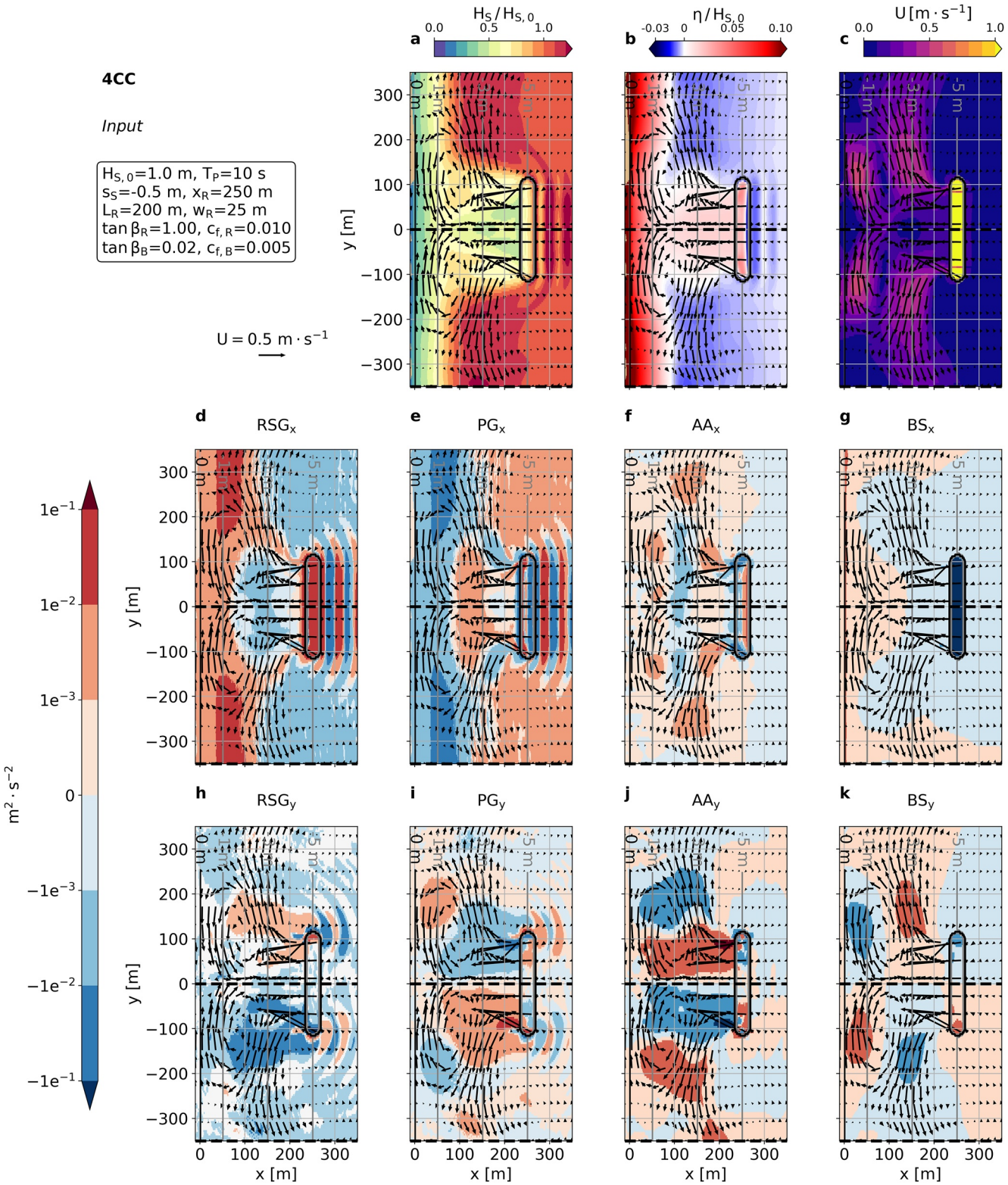

Figure 3.

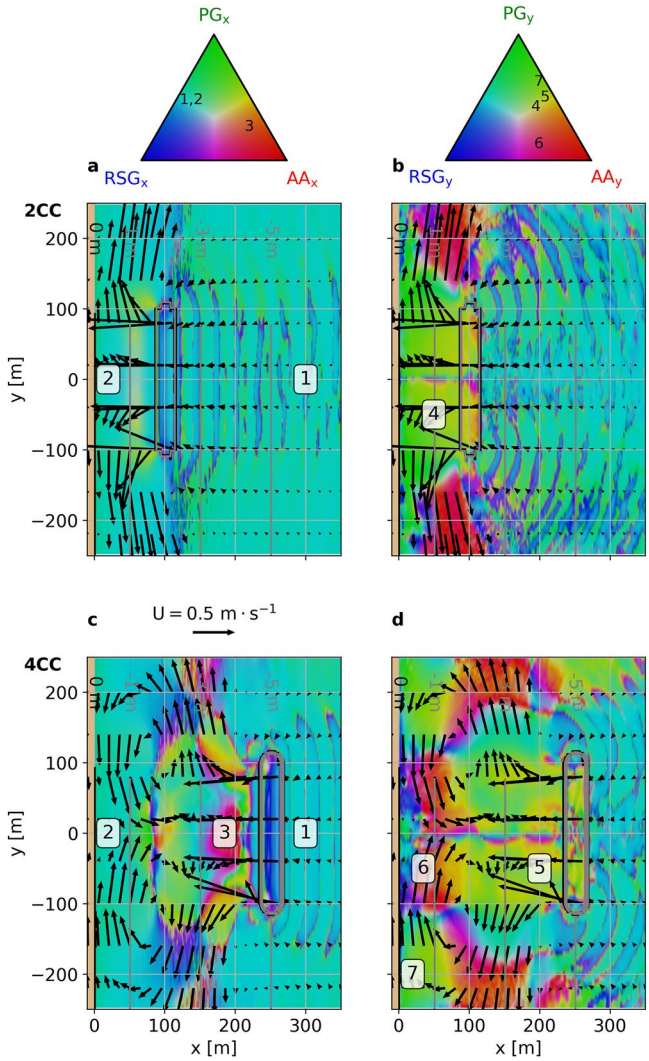

Figure 4. Map views of relative contribution of depth-integrated mean momentum terms for (a, b) a representative case of two-cell circulation (2CC) and (c, d) four-cell circulation (4CC) in (a, c) x- and (b, d) y-directions resulting from waves interacting with reefs. Vectors indicate the mass-flux velocities U_i whereas the (RGB) colors are calculated from the ratio of the absolute values of pressure gradients PG (green), advective acceleration AA (red), and radiation stress gradient RSG (blue), and the sum of their absolute values, normalized by their maximum values. The definition of each momentum term is given in Equation 1. The gray and black lines give the depth and reef contours, respectively. The numbered markers indicate key positions referenced in the text.

momentum balances, diverging (away from the reef) PG_y (Figure 2i) and converging (toward the reef) RSG_y (Figure 2h) are opposite in sign, with the former being larger in magnitude than the latter (marker four in Figure 4b). The net of PG_y and RSG_y is balanced by converging AA_y (Figure 2j) and diverging BS_y (Figure 2k), with the latter a response to the diverging currents (Figure 2c). The converging AA_y is dominated by the contribution from $(d + \langle\zeta\rangle)V\partial V/\partial y$ (not shown). For the 4CC, the diverging flows in the immediate lee of the reef ($100 < x < 230$ m) are qualitatively driven by similar dynamics to the 2CC (Figures 3h–3k; notice general dominance of PG_y represented by marker 5 in Figure 4d). However, close to the shoreline ($0 < x < 50$ m) converging currents develop due to different dynamics. Wave breaking over the exposed profile (breaking initiates at $x \sim 120$ m, Figures 5a and 3a, 3d) results in converging PG_y (Figures 5b and 3i) and also converging RSG_y (Figure 3h), with the former being generally larger in magnitude than the latter (marker seven in Figure 4d). Together with AA_y (Figure 3j), their net drives converging BS_y (Figure 3k) due to the converging mean currents (Figure 3c).

To evaluate the importance of each term in driving alongshore currents, we compared how the BS_y, which is assumed as a proxy for the mean alongshore currents (see Equation 9), can be described by the sum of different combinations of other terms in Equation 1 (e.g., Hansen et al., 2015). Specifically, we compared the sum of different terms and BS_y to the 1:1 line. The 1:1 line represents the perfect closure of the balance that occurs in case a given sum of terms exactly matches BS_y, therefore these terms drive alongshore flows. Linear slopes closer to one indicate better skill and lower errors, whereas R^2 close to one indicates less variance. To be able to represent the local balances, we used a regular output grid with x-grid and y-grid sizes of 4 m, and we considered the entire lee of reefs from $-L_R < y < L_R$ for the representative 2CC ($x < \sim$100 m) and 4CC ($x < \sim$250 m) cases. We first examined how well the net of PG_y and RSG_y, which typically dominate balances, represents BS_y (Figures 6a and 6b). The sum of PG_y and RSG_y is poorly correlated with BS_y ($R^2 = 0.1$–0.2), and the slopes of 1.53–1.70 indicate that accounting for $PG_y + RSG_y$ alone would overestimate the alongshore currents (Figures 6a and 6b). Including AA_y significantly improves the correlation ($R^2 \geq 0.67$, Figures 6c and 6d) and results in regression lines with slopes close to one (1.04–1.06), which demonstrates the overall importance of AA_y in the alongshore transfer of momentum. For the 4CC case, the advective acceleration AA_y is particularly important in the lee of the reef close to the shoreline ($20 < x < 100$ m; marker 6 in Figure 4d). The fact that a perfect correlation ($R^2 = 1$) necessitates the inclusion of the turbulent Reynolds stress gradients, $TRSG_y$, and hydrodynamic reaction at the bottom, HRB_y (Figures 6e–6h), establishes the importance of these terms for accurate local balances and attests to the complexity of the general balances. However, their importance for the overall alongshore flow dynamics is relatively limited due to their typically much lower magnitudes ($TRSG_y$ and HRB_y are of order 10^{-5} to 10^{-4} m^2 s^{-2} while BS_y is of order 10^{-3} m^2 s^{-2}).

Figure 3. Plan views of (a) normalized significant wave height $H_S/H_{S,0}$, (b) normalized setup $\eta/H_{S,0}$, (c) mass-flux velocity magnitude U, and (d–k) depth-integrated mean momentum terms for a representative case of four-cell circulation (4CC) resulting from waves interacting with reefs. In all panels, vectors indicate the mass-flux velocities U_i whereas colors indicate each variable. (d, h) Radiation stress gradient RSG in the x-(d) and y-(h) directions. (e, i) Pressure gradients PG in the x-(e) and y-(i) directions. (f, j) Advective acceleration AA in the x-(f) and y-(j) directions. (g, k) Bottom stresses BS_x in the x-(g) and y-(k) directions. The definition of each momentum term is given in Equation 1 and we note that the remaining terms had negligible contributions. The solid gray and black lines give the depth and reef contours, respectively. The dashed black lines give the reef center and exposed beach transects (see Section 4.1). The simulation input conditions are listed on the upper left table (see Figure 1 and Table 1 for definition of each variable).

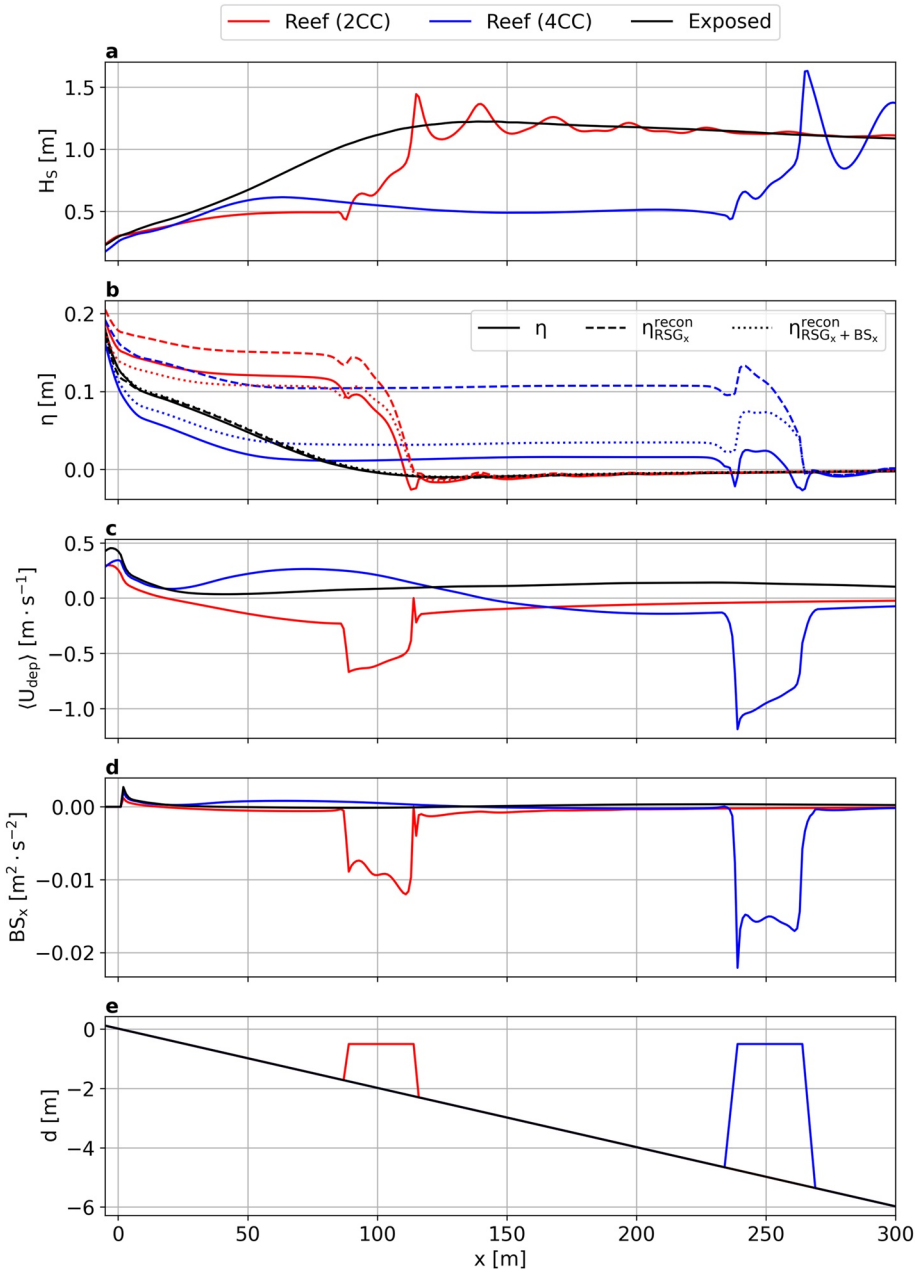

Figure 5. Cross-shore view of (a) significant wave height H_S, (b) setup η, (c) mean depth-averaged current $\langle U_{dep} \rangle$, (d) bottom stresses BS_x and (e) still water depth d at the reef center ($y = 0$ m) for the representative two-cell circulation (2CC, red lines; Figure 2) and four-cell circulation (4CC, blue lines; Figure 3) cases and at the exposed profile ($y = -L_R/2 - x_R$, black lines; note that we only show the exposed profile for the 4CC (black lines) because the 2CC and 4CC results were similar). In addition to the calculated shoreline setup (solid lines), the shoreline setup reconstructed by radiation stress gradients RSG_X (dashed lines) and net of RSG_X and bottom stresses BS_x (dotted lines) are also shown in (b). To reconstruct the shoreline setup η^{recon}, we assumed the balance between pressure gradients ($g(d+\eta)\frac{\partial \eta}{\partial x_i}$) and each forcing term (indicated as subscripts; i.e., RSG_x and BS_x) (see Section 4.1.1).

4.1.2.1. Alongshore Flow Dynamics Near the Shoreline

Here we conduct detailed analysis of the alongshore flow dynamics close to the shoreline, where the flow would more likely be able to drive sediment transport and coastal changes, and with which we can differentiate 2CC and 4CC cases. We calculated the cross-shore averaged values of the alongshore mass-flux velocities V (Figure 7a) and alongshore momentum terms from onshore (taken at $x = -10$ m) to a depth $d = 1$ m ($x < 50$ m), for the

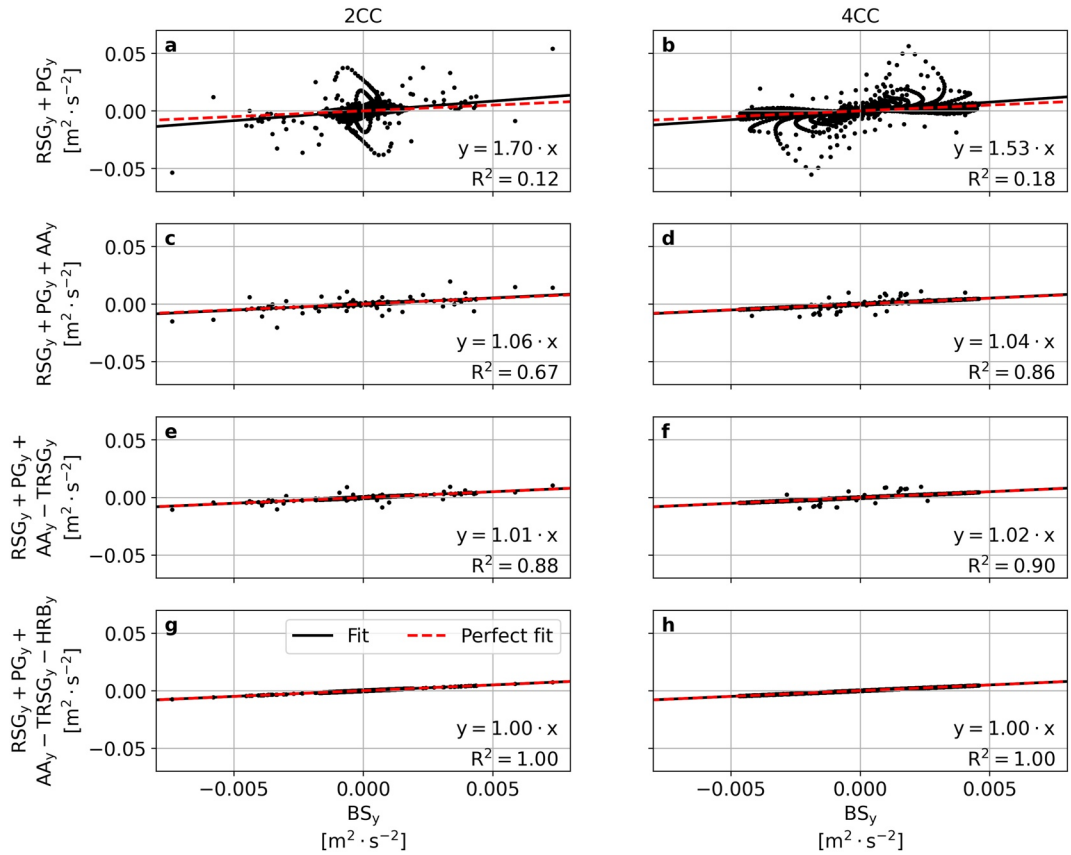

Figure 6. (a, b) Alongshore net forcing of radiation stress gradient RSG_y and pressure gradient PG_y versus bottom stresses BS_y for (a) the representative two-cell circulation (2CC) and (b) four-cell circulation (4CC) cases. In all panels each momentum term was calculated over the reef lee ($x < \sim$100 m for the 2CC and $x < \sim$250 m 4CC) and from $-200 < y < 200$ m (Figures 2 and 3), with the output from each grid cell shown (x-output and y-output grid sizes of 4 m). (c, d) Alongshore net forcing of RSG_y, PG_y and advective acceleration AA_y versus BS_y for the (c) 2CC and (d) 4CC cases. (e, f) Alongshore net forcing of RSG_Y, PG_y, AA_y, and turbulent Reynolds stresses gradients $TRSG_y$ versus BS_y for the (e) 2CC and (f) 4CC cases. (g, h) Alongshore net forcing of RSG_y, PG_y, AA_y, $TRSG_y$, and hydrodynamic reaction at the bottom HRB_y versus BS_y for the (g) 2CC and (h) 4CC cases. The black line provides the linear fit between each forcing and BS_y, whereas the red lines represent the perfect closure that occurs in case a given sum of terms exactly match BS_y. The definition of each momentum term is given in Equation 1.

representative 2CC (Figure 7b) and 4CC cases (Figure 7c) (note that we only show the lower part of the domain $y \leq 0$ m because results are symmetrical). The alongshore currents V for the representative 2CC had a similar parabolic pattern as BS_y (Figures 7a and 7b). For the 2CC (Figure 7b), the diverging PG_y are much larger in magnitude than converging RSG_y in the lee of the reef. The advective accelerations AA_y oppose PG_y and are larger than RSG_y in the reef lee. The gap between the location of maximum absolute V and PG_y reveals the role of RSG_y and AA_y in shifting the location where the maximum V is observed (where RSG_y peak) to about 15 m away from the reef. The net of PG_y, RSG_y, and AA_y is thus responsible for driving the converging BS_y.

The alongshore currents and bottom stresses of the 4CC case also display similar parabolic profiles (Figures 7a and 7c). Wave breaking over the exposed profile results in converging (negative) PG_y values that are always much larger than the also converging RSG_y values ($-200 < y < -115$ m) (Figure 7c). The net of PG_y and RSG_y drives converging BS_y. In the lee of the reef, PG_y values are close to zero, which result from averaging the diverging (farther offshore) and converging (closer to the shoreline) PG_y (Figure 3i). Therefore, the local driver of the converging currents in the lee of the reef is the net of AA_y and RSG_y. The fact that AA_y generally exceeds RSG_y and become the largest momentum term (marker six in Figure 4d) shows that currents in the lee of the reef are predominantly driven by momentum transported from the exposed region. While the combined effect of PG_y, RSG_y, and AA_y is crucial for predicting the local drivers of BS_y and currents, the converging currents are mainly driven by the converging PG_y resulting from wave breaking over the exposed profile (marker seven in Figure 4d). The remaining terms

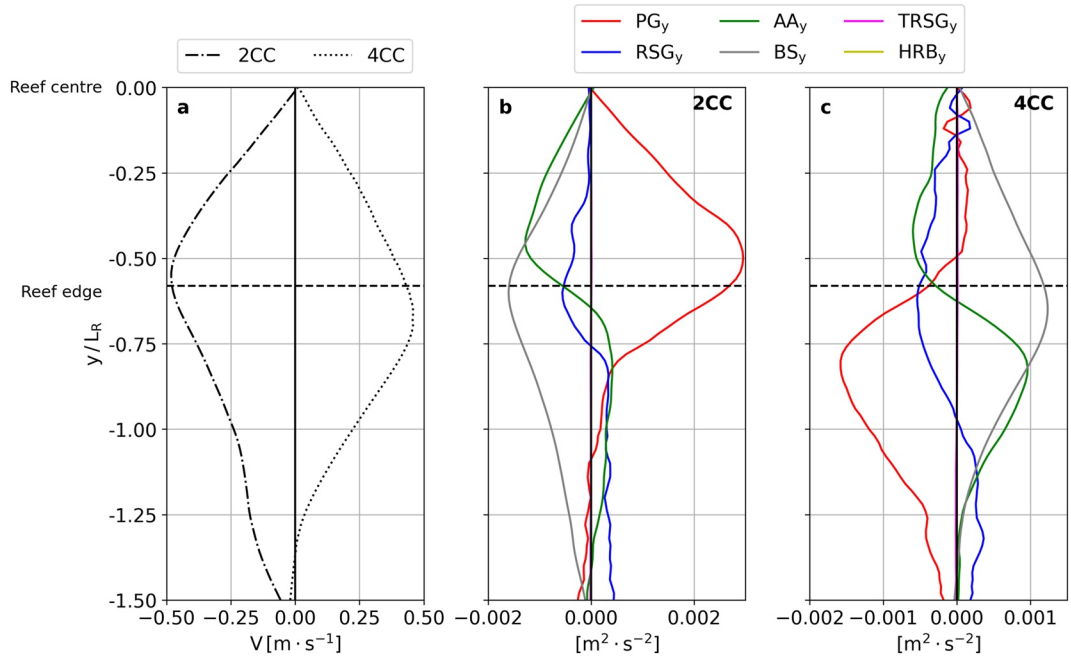

Figure 7. (a) Mean (over the cross-shore) of alongshore mass-flux velocity V as a function of alongshore location for the representative two-cell circulation (2CC, Figure 2) and four-cell circulation (4CC, Figure 3) cases. In all panels each momentum term was averaged from land until the still water depth $d = 1$ m ($x < 50$ m). (b, c) Mean (over the alongshore) of alongshore pressure gradient PG_y, radiation stress gradient RSG_y, advective acceleration AA_y, bottom stresses BS_y, turbulent Reynold stress gradient $TRSG_y$, and hydrodynamic reaction at the bottom HRB_y for the (b) 2CC and (c) 4CC cases. Note that we only show the lower half ($y < 0$ m) of the plot because results are symmetrical. The horizontal black line indicates the reef edge. The definition of each momentum term is given in Equation 1.

$TRSG_y$ and HRB_y had negligible contributions in both the 2CC and 4CC cases (Figures 7b and 7c). To conclude, despite the fundamental differences in their balances, the diverging and converging currents near the shoreline are ultimately primarily driven by the sign of PG_y near the shoreline. Accordingly, the differences between 2CC and 4CC cross-shore setup dynamics cause distinct alongshore flow patterns near the shoreline (see also Section 4.3).

4.2. Influence of Reef Properties and Beach Slope on Wave-Driven Flows

4.2.1. Reef Properties

Here we investigate how key reef properties, namely the reef friction coefficient $c_{f,R}$, reef distance to the shoreline x_R, reef base depth d_R, length L_R, and width w_R, influence the wave-driven flow patterns and relate these to the momentum dynamics. While a synthesis of how variations in these parameters influence the momentum dynamics and circulation patterns is presented here, a detailed set of figures showing how each parameter individually affects the flow dynamics can be found in the Supporting Information S1. The reef parameters $c_{f,R}$ (0.01–0.1), L_R (100–400 m), and w_R (10–50 m) were varied one at a time while holding the other reef parameters constant at the default values for each parameter ($c_{f,R} = 0.01$, $L_R = 200$ m, and $w_R = 25$ m). For each of these parameter variations, we ran two simulations with $x_R = 100$ and 250 m because of anticipated major role of x_R in modifying flow patterns (da Silva et al., 2022; Ranasinghe et al., 2006, 2010). With the linear beach slopes assumed in this section, x_R and d_R are exactly related. For these runs, we used identical wave conditions and default reef geometries as the 2CC and 4CC representative cases (Section 4.1 and Table 2). We quantified the response of the alongshore flows near the shoreline to alongshore setup gradients as follows. To assess the strength of the alongshore currents, we computed the square of maximum velocities $|V_M|V_M$ as an indicator for the circulation type and strength, based on the quadratic relationship that governs how bottom stresses $\tau_{B,i}$ scale with the alongshore flow velocities (Equation 9). Given that in the lee of reefs the mean bottom shear stresses $\langle \tau_{B,i} \rangle$ tend to be dominated by the contribution from mean currents (da Silva et al., 2022), using $|V_M|V_M$ is a reasonable proxy for BS_y. The alongshore currents were first averaged from land to $d = 1$ m ($x < 50$ m), and then the maximum currents V_M

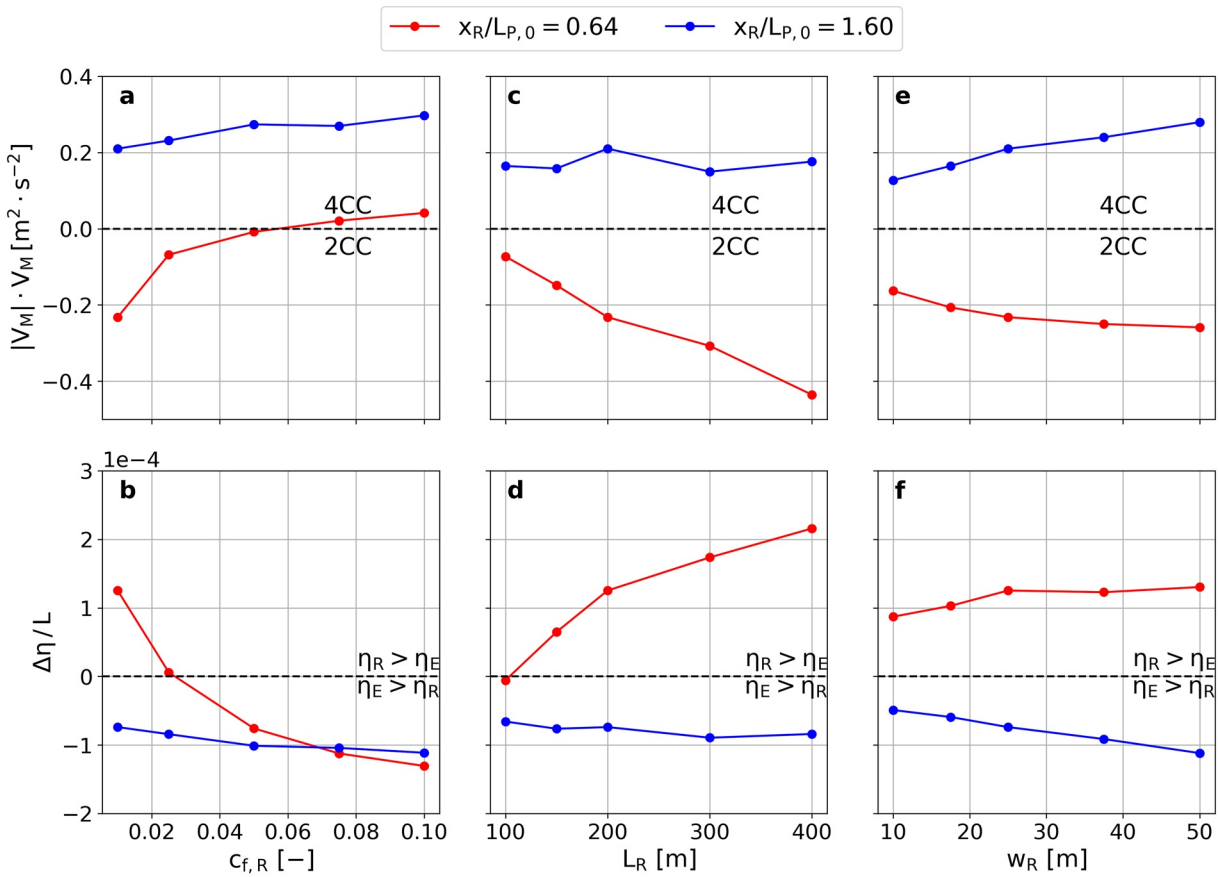

Figure 8. Effect of varying (a, b) reef friction coefficient $c_{f,R}$, (c, d) reef length L_R, and (e, f) width w_R on (a, c, e) square of cross-shore averaged (near the shoreline) alongshore mass-flux velocity $|V_M|V_M$ and (b, d, f) gradient between shoreline setup at the reef center and exposed beach $\Delta\eta/L$, where $\Delta\eta = \eta_R - \eta_E$ and $L = L_R/2 + x_R$. The colors distinguish results for two different reef distances to the shoreline x_R normalized by the deep water peak wavelength $L_{P,0}$. The shoreline setup was calculated at the still water depth $d = 0$ m (at $x = 0$ m). The reef and exposed profile alongshore positions were taken at $y = 0$ m and $-L_R/2 - x_R$, respectively. The alongshore mass-flux velocities V were first averaged from land until the still water depth $d = 1$ m ($x < 50$ m), then V_M was calculated where $|V|$ is maximum over the lower ($y < 0$ m) lee of the reef.

were calculated where their absolute values peaked. As we only included the lower part of the domain ($y < 0$ m) because patterns are symmetric, negative and positive $|V_M|V_M$ correspond to diverging (2CC) and converging (4CC) currents, respectively. Next, we calculated the gradient between the shoreline setup at the reef center and exposed beach $\Delta\eta/L$ as a proxy for the overall alongshore pressure gradient PG_y driving the alongshore currents, where $\Delta\eta = \eta_R - \eta_E$ and $L = L_R/2 + x_R$. The reference location for the exposed beach (given by the subscript E) was taken at $y = -L_R/2 - x_R$ (see Section 4.1.1). Note that changes in $\Delta\eta/L$ are primarily driven by variations in η_R because, under constant wave forcing and with fixed beach slope, η_E is approximately a constant irrespective of the varied reef properties.

Increased reef roughness ($c_{f,R}$) results in stronger converging flows $|V_M|V_M$ (Figure 8a) and reduced setup in the lee of the reef (η_R) (Figure 8b). Both the wave height and setup in the direct lee of the reef are reduced for larger $c_{f,R}$ (Figures S1c and S1d in Supporting Information S1), which is explained by the increase in the magnitude of BS_x (Figure S1d in Supporting Information S1) that enhances the sink of momentum. As bottom stresses increase over the reef, the setup in the reef lee becomes increasingly lower than at the exposed beach and thus drives an increasingly converging PG_y (Figure S1d in Supporting Information S1), which ultimately leads to a switch from a 2CC to a 4CC for the $x_R = 100$ m case (Figure 8a and Figure S1a in Supporting Information S1).

Changing the reef length L_R has two effects. For reefs close to the shoreline ($x_R = 100$ m), increased η_R (Figure 8d) and stronger diverging flows (Figure 8c) occur for increased L_R. Despite the nearly similar wave dissipation over the reef (Figures S2c and S2d in Supporting Information S1), the setup in its lee is larger for longer reefs. The setup dynamics at the reef center for longer reefs approach the mean balance typically observed in alongshore

uniform beaches case (i.e., between RSG_x and PG_x) due to the limited mass-flux atop the reef and decrease in magnitude of BS_x (Figure S2e in Supporting Information S1). Due to the increased path length for water behind a longer reef to flow back to the ocean, which results in increased integration of the bottom stress, the setup at the reef center becomes increasingly larger than at the exposed beach, which results in stronger diverging PG_y that ultimately drive stronger diverging currents (Figures S2a and S2b in Supporting Information S1). For reefs situated in deeper waters ($x_R = 250$ m), L_R had little effect on the alongshore circulation (Figure 8c, blue lines). Despite the increased setup immediately behind longer reefs (Figure S2d in Supporting Information S1), shorter reefs experience an increase in wave heights in the lee of the reef owing to alongshore fluxes of wave energy behind the reef (e.g., due to diffraction, Figure S2c in Supporting Information S1) that ultimately led to similar setup at the shoreline and no significant changes to the alongshore circulation.

Reefs with wider cross-shore widths w_R experience an increase in current magnitude, with stronger diverging and converging flows for reefs situated in shallower and deeper waters, respectively (Figures 8e and 8f, red lines). For reefs with $x_R = 100$ m, wider reefs result in increased wave dissipation and increased setup in the lee (Figures S3c and S3d in Supporting Information S1). Despite the increase in BS_x (Figure S3e in Supporting Information S1), the setup is larger for wider shallow reefs because of greater dissipation by wave breaking. Consequently, larger diverging PG_y will drive stronger diverging currents near the shoreline (Figures S3a and S3b in Supporting Information S1). For reefs with $x_R = 250$ m, wider reefs also experience increased wave dissipation and increased setup immediately behind the reef (Figures S3c and S3d in Supporting Information S1). Yet, larger setup occurs for narrower reefs because at the second break point close to the shoreline ($x < 50$ m) wave heights are larger due to less dissipation occurring over the reef. Consequently, for $x_R = 250$ m, an increase in the reef width w_R results in stronger converging PG_y that drive increased converging currents near the shoreline (Figures S3a and S3b in Supporting Information S1).

Overall, the four reef parameters x_R, L_R, w_R, and $c_{f,R}$ influence the setup in the lee of the reef and are important for the alongshore flow dynamics. However, for the cases modeled, x_R and $c_{f,R}$ were the only reef variables with the ability to modify the circulation pattern from a 2CC into a 4CC while keeping the remaining parameters constant, which suggests their key role in the flow dynamics.

4.2.2. Beach Slope

Here we evaluate the influence of the beach slope in influencing the flow dynamics. We analyzed how changing beach slopes influence $|V_M|V_M$ and $\Delta\eta/L$ (see Section 4.2.1). We varied the slope ($\tan\beta_B = 0.01$–0.05) while keeping both x_R and s_R constant, which resulted in varying d_R (2–12.5 m). For each slope variation, we ran two simulations with $x_R = 100$ and 250 m. All other parameters were fixed and similar to the 2CC and 4CC representative cases (see Section 4.1). To calculate $|V_M|V_M$, the alongshore currents were first averaged from land to $d = 1$ m (unlike in previous sections, a fixed depth and varying slopes result in $x < 1/\tan\beta_B$), and then the maximum currents V_M are calculated where the absolute values peaked.

The results show that steeper slopes (or larger $\tan\beta_B$) result in increased η_E (e.g., Raubenheimer et al., 2001) owing to larger RSG_x. The changes in η_E in response to varying slope generally influence $\Delta\eta/L$ more than the changes in η_R (not shown). Steeper slopes yield increased η_E and reduced $\Delta\eta/L$ (Figure 9b), which are consistent with stronger converging PG_y (Figure S4b in Supporting Information S1) that drive increased converging currents (Figure 9b and Figure S4a in Supporting Information S1). Increased x_R (or d_R, see top x axis of Figure 9) at a given slope results in stronger converging flows (Figure 8a and Figure S4a in Supporting Information S1). While for most cases this response is due to the reduction in $\Delta\eta/L$, for the steepest slopes ($\tan\beta_S > 0.03$) both $\Delta\eta/L$ and PG_y are lower for reefs situated with lower x_R. The fact that lower $\Delta\eta/L$ yields lower converging currents can be explained by the larger area available for the development of alongshore currents for cases with larger x_R (i.e., with less influence of the diverging currents). Overall, these results indicate that the beach slope and the dependent parameters x_R and d_R have a major influence in the setup and alongshore circulation dynamics. For a given set of wave conditions and reef parameters, a change in slope can modify the circulation pattern from a 2CC into a 4CC, which makes it a key parameter in the alongshore flow dynamics.

4.3. Synthesis of Drivers of Reef Circulation Patterns Subject to Variable Hydrodynamic Forcing

In this section, we collectively consider the results from the broad range of simulations together to identify the most significant features of the overall flow dynamics that differentiate the 2CC and 4CC patterns generally. Unlike in previous sections, where we studied how reef parameters and slopes individually affect the momentum dynamics, here we synthesize and analyze a comprehensive set of simulations including permutations of $H_{s,0}$,

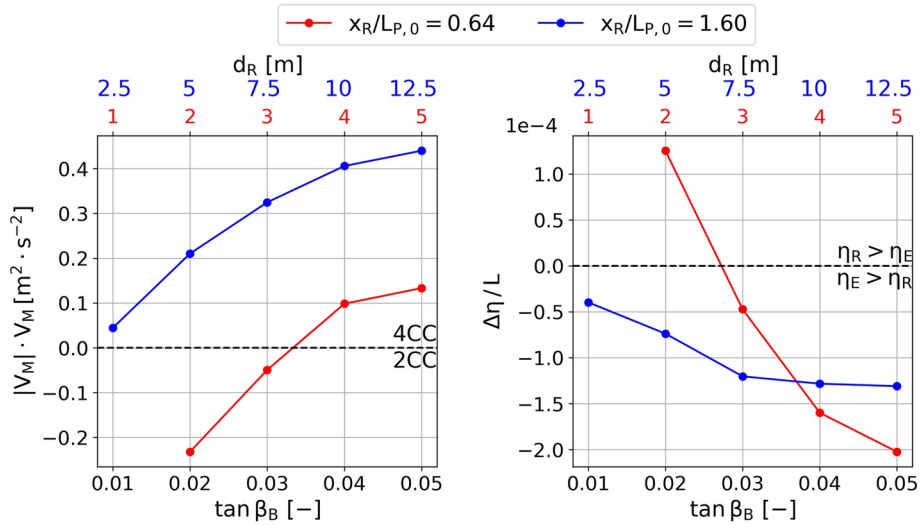

Figure 9. Effect of varying beach slope ($\tan\beta_B$; where steep/mild slopes are indicated by large/small $\tan\beta_B$ values, respectively) on (a) square of cross-shore averaged (near the shoreline) alongshore mass-flux velocity $|V_M|V_M$ and (b) gradient between shoreline setup at the reef center and exposed beach $\Delta\eta/L$, where $\Delta\eta = \eta_R - \eta_E$ and $L = L_R/2 + x_R$. The colors distinguish results for two different reef distances to the shoreline x_R normalized by the deep water peak wavelength $L_{P,0}$. The upper x axis indicates the reef base depth d_R for each x_R. The shoreline setup was calculated at the still water depth $d = 0$ m (at $x = 0$ m). The reef and exposed profile alongshore positions were taken at $y = 0$ m and $-L_R/2 - x_R$, respectively. The alongshore mass-flux velocities V were first averaged from land until the still water depth $d = 1$ m ($x < 1/\tan\beta_B$), then V_M was calculated where $|V|$ is maximum over the lower ($y < 0$ m) lee of the reef.

T_P, s_R, x_R, d_R, L_R and w_R across our parameter space (Table 2) while keeping a fixed reef friction coefficient $c_{f,R} = 0.01$ and beach slope $\tan\beta_B = 1/50$ due to computational constraints.

4.3.1. Alongshore Drivers

Here we use the full database of simulations to assess common features of the alongshore variation of alongshore mass-flux velocities and momentum terms. First, we averaged V, PG_y, RSG_y, and AA_y close to the shoreline (same region as before, see Section 4.1); next, we normalized each by the maximum values of each simulation $|V|_{max}$ and $|F|_{max}$, which were calculated where their absolute values peak. The momentum terms are normalized by $|F|_{max}$ based on the maximum forcing term value among PG_y, RSG_y, and AA_y. We grouped simulations into 2CC (Figure 10b) and 4CC (Figure 10c) classes based on the direction of the maximum absolute alongshore currents occurring in the lee of the reef (in the lower part of the domain 2CC and 4CC occur for negative and positive currents, respectively). The normalized alongshore currents and momentum terms patterns display similar alongshore variations as was observed for the representative 2CC and 4CC (Figure 10). Overall, this analysis indicates the magnitude and structure of the alongshore pressure gradients are the primary factors determining whether the flow is 2CC or 4CC. Next, we analyzed how the parameter space considered influences the setup profiles both over the reef center and at the exposed area by computing the correlation between $\Delta\eta/L$ and $|V_M|V_M$ (see Section 4.2 for details). Diverging (red in Figure 11) and converging (blue) currents generally develop for $\eta_R > \eta_E$ and $\eta_R < \eta_E$, respectively. For diverging currents, $|V_M|V_M$ highly correlates with $\Delta\eta/L$ (red line, $R^2 = 0.93$), whereas for converging currents a moderate correlation is observed (blue line, $R^2 = 0.43$). The stronger correlation for diverging currents is consistent with the well-defined alongshore momentum balance patterns and stronger dominance of PG_y for the 2CC cases (Figure 10b) than for the 4CC cases (Figure 10c). Overall, these results indicate that knowledge of the shoreline setup onshore of the reef center and at the exposed profile can be used to reasonably determine whether a 2CC or 4CC will occur.

4.3.2. Setup Dynamics

Due to the importance of the magnitude of setup generation behind the reef to the alongshore flow dynamics, the study of the cross-shore setup balance allows us to identify the physical processes that create the 2CC and 4CC patterns. To understand the role of different cross-shore momentum terms in driving the shoreline setup at the reef center and exposed beach, we reconstructed the setup at these two locations first with RSG_x ($\eta^{recon}_{RSG_x}$) and last with $RSG_x + BS_x$ ($\eta^{recon}_{RSG_x+BF_x}$; the same approach used in Section 4.1.1). The setup generation by wave breaking

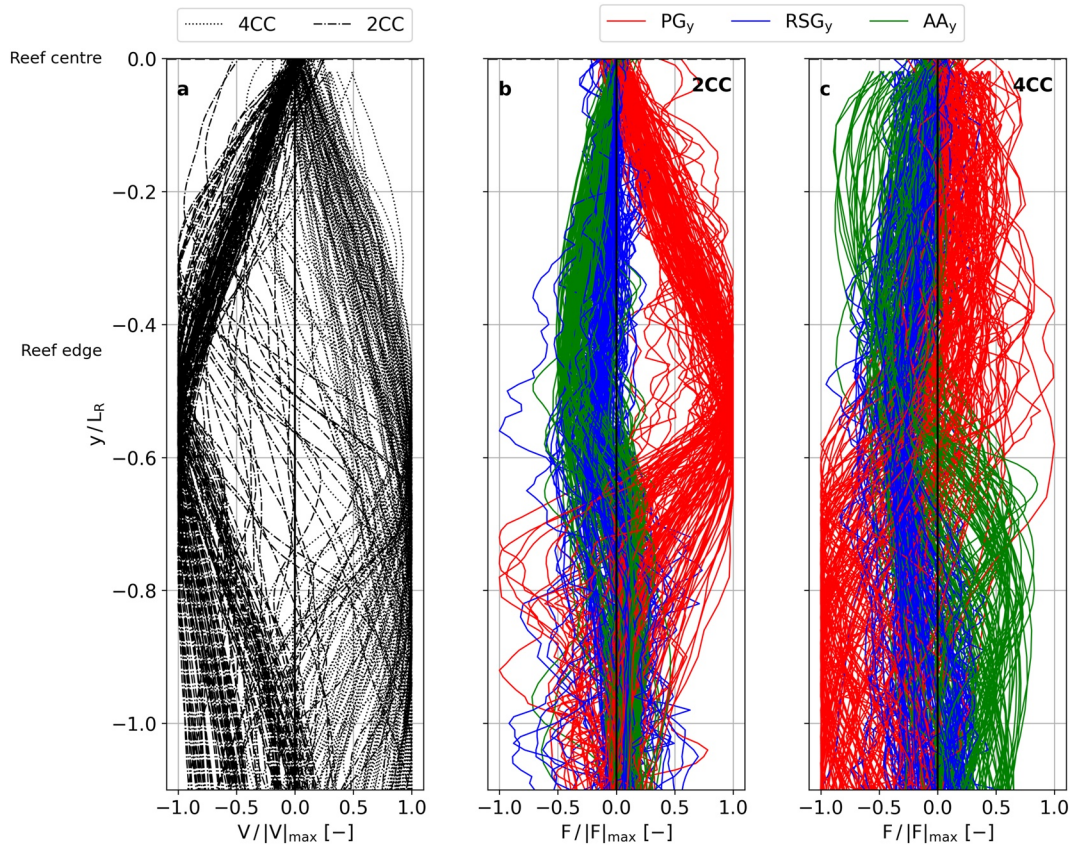

Figure 10. (a) Mean (over the cross-shore) of alongshore mass-flux velocity V normalized by absolute value of maximum $|V|_{max}$ as a function of alongshore location normalized by the reef length y/L_R for a range of modeling cases (see text for model input files). (b, c) Mean (over the cross-shore) of alongshore pressure gradient PG_y, radiation stress gradient RSG_y, and advective acceleration AA_y, each normalized by the maximum absolute forcing term $|F|_{max}$. Note that we only show the lower half ($y < 0$ m) of the plot because results are symmetrical. The horizontal black line indicates the reef edge. In all panels velocities and momentum terms were averaged from land until the still water depth $d = 1$ m ($x < 50$ m). The classification into 2CC and 4CC in (a) was based on the direction of the maximum absolute alongshore currents occurring in the lee of the reef (i.e., $\sim -0.5 \leq y/L_R \leq 0$). The definition of each momentum term is given in Equation 1.

(η^{recon}_{R,RSG_x}, i.e., predicted only by RSG_x) is highly correlated with the actual setup behind the reef η_R ($R^2 = 0.76$); however η_R is on average overestimated ($RB = 36\%$, where RB stands for relative bias, Figure 12a). The reconstructed setup with $RSG_x + BS_x$ ($\eta^{recon}_{R,RSG_x+BF_x}$) yield accurate setup estimates (Figures 12a and 12b), which indicates that including BS_x is essential for correctly calculating η_R (e.g., Figure 5b). The seaward BS_x associated with the onshore flows over the reef (e.g., Figures 5c and 5d) reduces the wave setup. At the exposed beach, the setup generation by wave breaking (η^{recon}_{E,RSG_x}) accurately reproduces the setup ($RB = -6\%$, Figure 12c). The setup prediction is increased with $RSG_x + BS_x$ ($\eta^{recon}_{E,RSG_x+BF_x}$) and the negative bias is removed ($RB = 1\%$), consistent with the shoreward BF_x associated with undertow near the shoreline enhancing wave setup (e.g., Figures 5c and 5d). Next, we calculated the reconstructed and actual difference between the setup at the reef and exposed beach $\Delta\eta$ with the same forcing terms (Figures 12e and 12f). Despite the high correlation between the $\eta^{recon}_{RSG_x}$ at the two locations, the reconstructed $\Delta\eta$ with RSG_x ($\Delta\eta^{recon}_{RSG_x}$) has poor correlation ($R^2 = 0.18$) and a bias of $\sim -200\%$ (Figure 12e). As $\Delta\eta^{recon}_{RSG_x}$ results in nearly always positive values (i.e., $\eta^{recon}_{R,RSG_x} > \eta^{recon}_{E,RSG_x}$), the alongshore pressure gradients based on $\eta^{recon}_{RSG_x}$ would generally result in diverging currents. The reconstructed $\Delta\eta$ with $RSG_x + BS_x$ ($\Delta\eta^{recon}_{RSG_x+BF_x}$) provides increased correlation ($R^2 = 0.80$) and much reduced bias ($RB = -25\%$, Figure 12f), which indicates that the alongshore pressure gradients predicted by $\eta^{recon}_{RSG_x+BF_x}$ would provide reasonable estimates of the actual forcing that drives 2CC and 4CC systems. The perfect representation of $\Delta\eta$ (i.e., with $R^2 \sim 1$) requires reconstructing the setup by also including the advective acceleration AA_x and turbulent Reynolds stress gradients $TRSG_x$ (not shown).

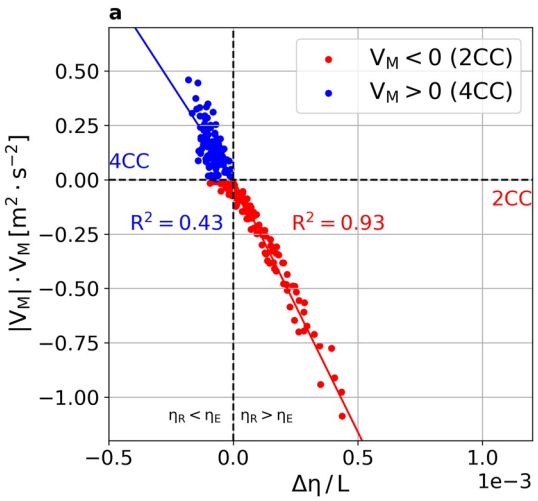

Figure 11. Square of cross-shore averaged (near the shoreline) alongshore mass-flux velocity $|V_M|V_M$ versus gradient between shoreline setup at the reef center and exposed beach $\Delta\eta/L$, where $\Delta\eta = \eta_R - \eta_E$ and $L = L_R/2 + x_R$, for a range of modeling cases (see text for model input files). The solid blue and red lines indicate the linear fit between $|V_M|V_M$ and $\Delta\eta/L$ for converging ($V_M > 0$ m s^{-1}) and diverging ($V_M < 0$ m s^{-1}) currents, respectively. The shoreline setup was calculated at the still water depth $d = 0$ m (at $x = 0$ m). The reef and exposed profile alongshore positions were taken at $y = 0$ m and $-L_R/2 - x_R$, respectively. The alongshore mass-flux velocities V are averaged from land until the still water depth $d = 1$ m ($x < 50$ m), then V_M is calculated where $|V|$ is maximum over the lower ($y < 0$ m) lee of the reef.

5. Discussion

5.1. Circulation Dynamics

Through an analysis of momentum balances that govern the wave-driven circulation patterns in the lee of nearshore reef systems, our study demonstrated that the occurrence of 2CC and 4CC flow patterns are determined by distinct momentum balances that are established in different areas in the lee of the reef. The diverging and converging currents originate from wave breaking over the reef and at the adjacent exposed profile, respectively. The breaking over the reef results in diverging pressure gradients PG_y and converging radiation stress gradients RSG_y, and because $|PG_y| > |RSG_y|$ diverging currents emerge directly in the lee of the reefs both for 2CC and 4CC. For the 2CC, this diverging current pattern extends to the shoreline. For the 4CC, although the area directly in the lee of the reef is also characterized by diverging currents, the wave breaking over the exposed profile at a distance from the shoreline results in converging PG_y and RSG_y that together drive converging currents onshore of the diverging currents up to the shoreline. Although the relative importance of each momentum term governing local balances varies and their accurate description requires most terms, the overall alongshore flow patterns (i.e., 2CC or 4CC) are largely driven by PG_y, which confirms the hypothesis made in previous studies (e.g., Ranasinghe et al., 2006; Villani et al., 2012). Given the critical role that the alongshore pressure gradient PG_y plays in describing the magnitude and direction of alongshore flows, the difference between the setup profiles over the reef center and at the adjacent exposed beach was found to correlate with alongshore currents near the shoreline. The strong influence of reef length on the shoreline setup demonstrates that alongshore wave propagation (e.g., due to diffraction) and alongshore currents need to be considered for an accurate description of the setup dynamics.

The key aspects of the overall flow dynamics in the lee of nearshore reef systems can be explained by the cross-shore setup dynamics over the reef-fronted and exposed beaches. In general, shoreline setup at the reef center that is lower or larger than at the exposed beach will result in converging and diverging currents, respectively. The cross-shore momentum balance analysis indicates that the shoreline setup mainly results from the forces associated with the wave breaking and onshore flows over the reef. Through the seaward bottom stresses (a response to the onshore flows over the reef), reef roughness can substantially reduce the setup generation by wave breaking. The setup that would be predicted by considering radiation stress gradients alone (i.e., neglecting bottom stresses) results in larger shoreline setup at the reef center than at the exposed beach, which would result in diverging pressure gradients that would drive diverging currents for nearly all cases. Consequently, including an accurate representation of the bottom stresses is fundamental for describing the dynamics of 2CC or 4CC patterns.

Reefs can be present in nature with a wide range of different roughness properties. Our study showed that variations of the reef friction coefficient substantially influence the alongshore flow dynamics. Rougher reefs are more prone to develop 4CC owing to decreased shoreline setup at the reef-fronted beach. We used a range of $c_{f,R}$ based on mean currents (Rosman & Hench, 2011) to represent bottom shear stresses. However, in SWASH bottom stresses are calculated based on the instantaneous flows, independent of whether they are driven by mean currents or wave-driven oscillatory flows, which does account for how the relationship between bottom stresses and near-bed flows that depends on the frequency of the motion (Lowe et al., 2005). Therefore, an optimal $c_{f,R}$ is likely to be different than that for mean flows alone. Limited studies to our knowledge have attempted to quantify reef friction coefficients $c_{f,R}$ based on instantaneous velocities (e.g., Buckley et al., 2016), and thus this is suggested as a potential area of future research as to provide drag coefficients relevant to combined mean and oscillatory flows (at intrawave timescales) across a range of sea floor environments. This would provide greater confidence in the selection of drag coefficients, particularly given their importance in determining the flow dynamics demonstrated here.

Although an extensive parameter space of reef properties was considered in these simulations, the effect of variable frictional properties of the surrounding beach were not considered (the friction coefficient of beach,

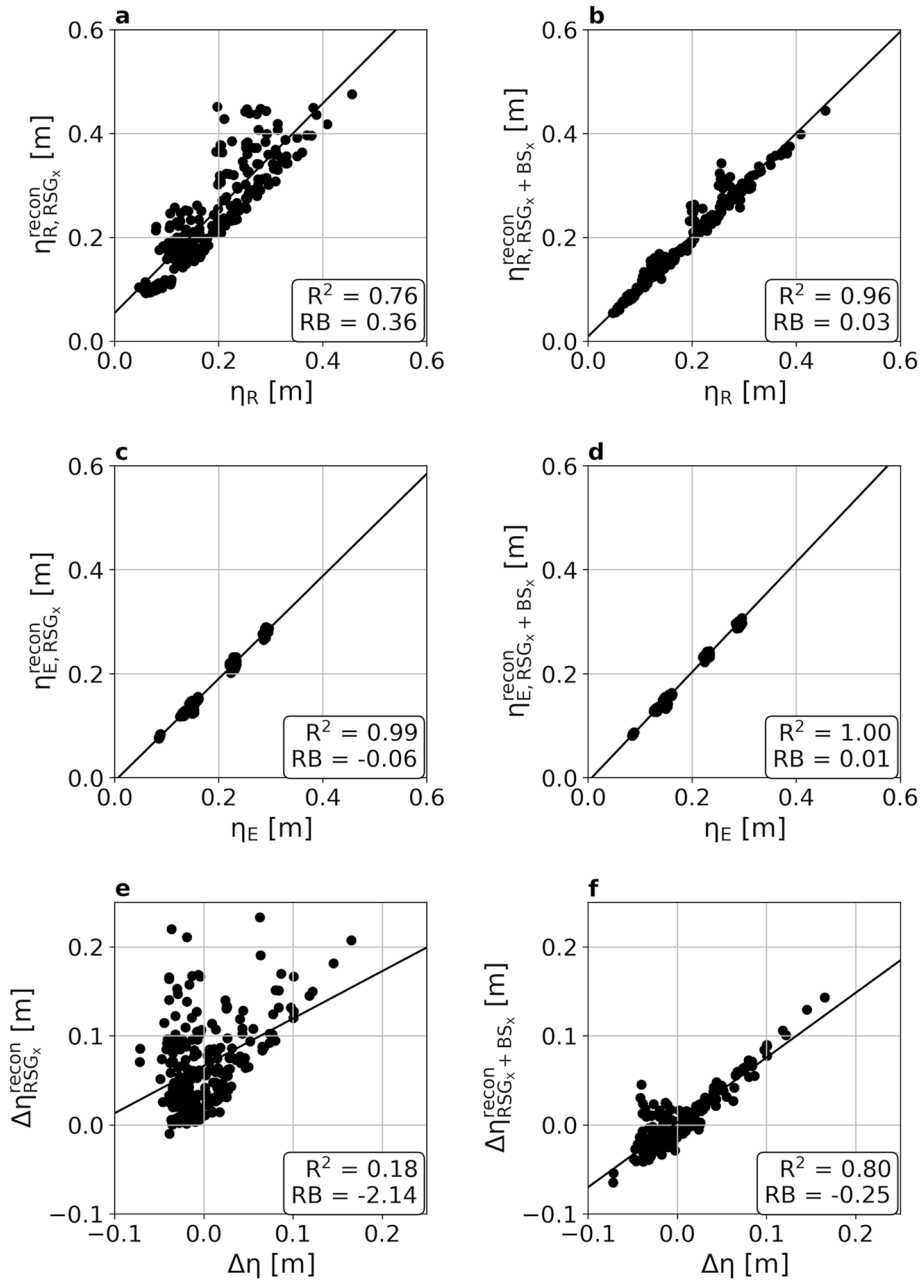

Figure 12. Comparison between reconstructed η^{recon} and modeled shoreline setup η at the (a, b) reef center (η_R, calculated at $y = 0$ m) and (c, d) exposed beach (η_E, calculated at $y = -L_R/2 - x_R$), and (e, f) reconstructed $\Delta\eta^{recon} = \eta_R^{recon} - \eta_E^{recon}$ and modeled $\Delta\eta = \eta_R - \eta_E$ for a range of modeling cases (each dot corresponds to a single run; see text for model input files). In all panels RB indicates the relative bias. The shoreline setup was calculated at the still water depth $d = 0$ m (at $x = 0$ m). To reconstruct the shoreline setup, we assumed the balance between pressure gradients ($g(d+\eta)\frac{\partial\eta}{\partial x}$) and each forcing term (indicated as subscripts; (a, c, e) RSG_x; (b, d, f) $RSG_x + \mathrm{BS_x}$, where RSG_x and $\mathrm{BS_x}$ indicate the cross-shore radiation stress gradients and mean bottom stresses, respectively; see Section 4.1.1).

$c_{f,B} = 0.005$, consistent with sand, was held constant across all simulations). Accordingly, the changes to the alongshore pressure gradients near the shoreline were mainly driven by the variations of the shoreline setup at the reef-fronted beach, rather than the setup at the exposed beach. The beaches surrounding reefs can vary in nature, which can influence the flow dynamics. In case the surrounding beaches have rougher beds (e.g., rocky beds or with bed forms), increased $c_{f,B}$ would likely increase the shoreline setup at the adjacent beach through the increased shoreward bottom stresses reacting to the undertow near the shoreline. As a result, rougher surrounding

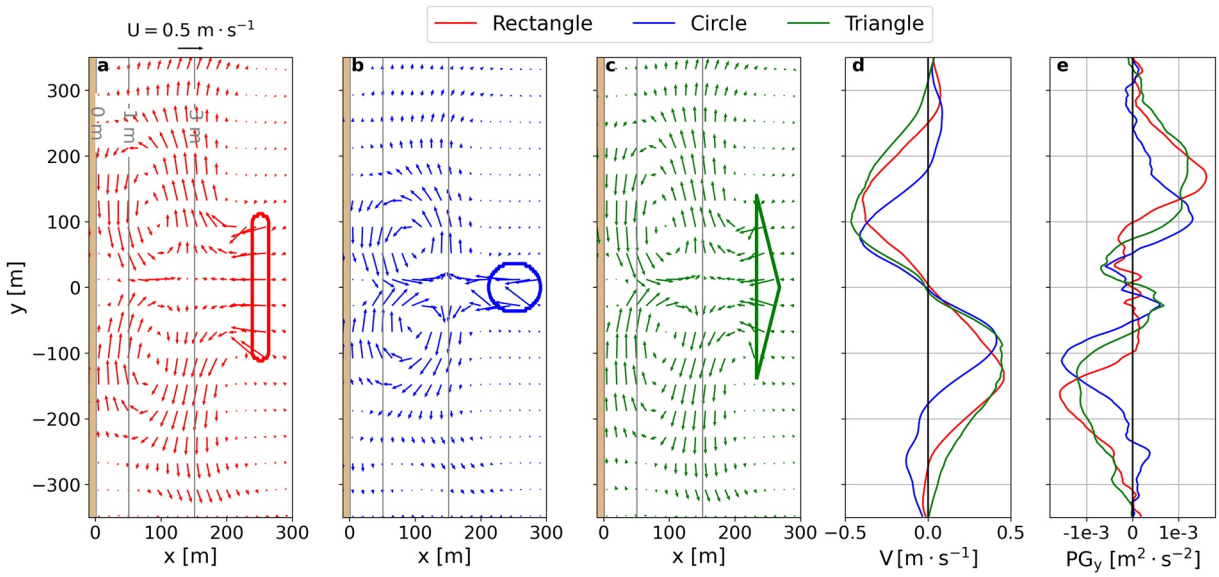

Figure 13. Map views of (a–c) mass-flux velocities U_i, mean (over the cross-shore) of (d) alongshore currents V and (e) alongshore pressure gradients PG_y resulting from waves interacting with rectangular (red), circular (blue), and triangular (green) shaped reefs with similar areas. The gray and red/blue/green lines give the depth and reef contours, respectively. Alongshore velocities and pressure gradients terms were averaged from land until the still water depth $d = 1$ m ($x < 50$ m). The input conditions were similar to the representative four-cell circulation (4CC, Figure 3), except for the reef shape.

beaches would have further increased the likelihood of developing a 4CC pattern because of stronger converging alongshore pressure gradients near the shoreline.

5.2. Influence of Reef Shape

The geometry of natural reefs can vary substantially which makes their idealized representation challenging. For simplicity, we considered rectangular-shaped reefs in our study. To evaluate whether the wave-driven flows are sensitive to varying reef shapes, we conducted exploratory modeling with two alternative crest shapes, circular, and triangular (isosceles) and compared them with the rectangular reefs while keeping the location and crest area constant for every reef shape. We used the same wave conditions and remaining reef parameters as the representative 4CC case (see Section 4.1). Despite some local differences in the flow patterns, the general aspects of the wave-driven circulation are similar for rectangular, circular, and triangular-shaped reefs (Figures 13a–13c). Because the shapes had little influence on the alongshore pressure gradients (Figure 13e), which mainly drive the alongshore currents, the alongshore currents near the shoreline were similar (Figure 13d). Consequently, these results suggest that using different reef geometrical shapes would likely have limited influence on the overall alongshore flow dynamics.

5.3. Implications for Shoreline Processes

The interactions between waves and nearshore reefs result in 2CC and 4CC patterns. The alongshore gradients in the sediment transport associated with diverging (2CC) and converging (4CC) currents near the shoreline would likely drive shoreline erosion and accretion, respectively (da Silva et al., 2022; Ranasinghe et al., 2006). Among the variety of reef properties, the reef distance to shoreline x_R, reef friction coefficient $c_{f,R}$, and beach slope $\tan\beta_B$ were found to have the most significant influence on the flow dynamics. Rougher reefs located farther away from the shoreline (or deeper) in steeper beaches are more prone to develop 4CC patterns generally because of reduced setup at the reef center that yields converging pressure gradients. Accordingly, these reef systems would more likely experience accreted shorelines behind a reef.

Reefs are present in a variety of coastal environments that experience a range of wave and water level conditions. As this forcing varies over time, it is possible for these circulation patterns behind natural reefs to substantially change during different periods (including alternating between 2CC and 4CC patterns) that may result in cycli-

cal patterns of shoreline erosion and accretion in the lee of reefs. With most studies of the shoreline responses to reefs having focused on the equilibrium shoreline response as a function of reef geometry (e.g., Black & Andrews, 2001), the dynamic nature of the shoreline position in the lee of small reefs remains largely unknown, with only a few exceptions (Duarte Nemes et al., 2019; Segura et al., 2018). For example, a study of a nearshore rocky reef system at Garden Island, Western Australia, found that the size of the salient (i.e., a seaward extension of the shoreline) behind reefs and at the adjacent embayment oscillated seasonally as a function of water levels and wave heights (Segura et al., 2018). While a detailed description of sediment transport patterns is required for better appraisal of the physical mechanisms driving the shoreline dynamics, this study may help to explain the cyclical behavior of the shoreline variability behind the reefs in response to seasonal variations in offshore sea level and wave conditions at that site. Results from the present study can explain some of the mechanisms by which temporal variations in hydrodynamic forcing conditions may influence the flow dynamics of nearshore reef systems and shoreline morphology. Larger oscillations of water levels, such as generated by large tidal ranges or seasonal sea level variations, would result in oscillating reef crest submergence. During periods with lower water levels, the wave breaking over reefs would yield 2CC or 4CC depending on the reef geometry. Reefs may become emergent and result in 4CC (e.g., da Silva et al., 2022; Suh & Dalrymple, 1987) and likely accretion in their lee. Increased water levels, which in the long-term may also be caused by sea level rise, could eventually inhibit or reduce depth-limited breaking over the reefs. In this case, the main hydraulic function of reefs would be to promote wave refraction, and the resulting alongshore-varying wavefield would yield alongshore-varying circulation forcing (e.g., Hansen et al., 2015). However, the decrease in the forcing may cause reduction of the strength of the alongshore currents (e.g., da Silva et al., 2022) and yield reduced sediment transport. The weakening of the mean flows that previously contributed to maintain erosion or accretion (e.g., salient) behind reefs would result in straightening of shorelines.

6. Conclusions

We conducted a detailed analysis of the momentum balances responsible for establishing 2CC and 4CC patterns in the lee of small nearshore reefs using a phase-resolved numerical model (SWASH) that incorporated a wide range of wave and water level conditions, reef properties, and beach slopes. The spatial variability of the pressure gradients and radiation stress gradients were responsible for driving the mean currents, which were countered by mean bottom stresses and advective accelerations. While the local balances significantly vary, the alongshore currents observed in 2CC and 4CC systems mainly resulted from diverging and converging alongshore pressure gradients that originate from the wave breaking over the reef and exposed profile, respectively. Rougher reefs situated in deeper waters (and farther away from the shoreline) were more prone to experience lower shoreline setup in their lees, which increases the likelihood of developing alongshore pressure gradients directed toward the reef center that drive 4CC systems. Through analysis of the cross-shore setup dynamics, we found that the setup on the reef profile developed in response to the net contribution of radiation stress gradients generated by wave breaking and mean bottom stresses associated with the strong onshore flows over the reefs. For 2CC cases, the reduction of setup by seaward bottom stresses was generally limited, which resulted in shoreline setup at the reef center that was larger than at the exposed beach. For the 4CC cases, the reduction of the setup by seaward bottom stresses resulted in shoreline setup at the exposed beach being larger than at the reef center.

Data Availability Statement

The numerical model input files for the representative two-cell and four-cell circulation cases are publicly available at https://doi.org/10.26182/1h84-7268.

Acknowledgments

This project forms part of a Ph.D. study by R.F.S. at the University of Western Australia which is supported by the Commonwealth Government through an Australian Government Research Training Program Scholarship. Parts of this research were also supported by the Marine Energy Research Australia through funding provided by the Western Australian Government, via the Department of Primary Industries and Regional Development (DPIRD), and University of Western Australia. Additional support was also provided from Australian Research Council (Discovery Project DP200101545 and Linkage Project LP210100386). This work was also supported by resources provided by the Pawsey Supercomputing Centre with funding from the Australian Government and the Government of Western Australia. We thank the Editor Ryan Mulligan and the two anonymous reviewers for the constructive reviews that improved this manuscript. Any use of trade, firm, or product names is for descriptive purposes only and does not imply endorsement by the U.S. Government. Open access publishing facilitated by The University of Western Australia, as part of the Wiley - The University of Western Australia agreement via the Council of Australian University Librarians.

References

Apotsos, A., Raubenheimer, B., Elgar, S., & Guza, R. T. (2008). Wave-driven setup and alongshore flows observed onshore of a submarine canyon. *Journal of Geophysical Research*, *113*, C07025. https://doi.org/10.1029/2007JC004514

Bellotti, G. (2004). A simplified model of rip currents systems around discontinuous submerged barriers. *Coastal Engineering*, *51*(4), 323–335. https://doi.org/10.1016/j.coastaleng.2004.04.001

Black, K., & Andrews, C. (2001). Sandy shoreline response to offshore obstacles: Part 1. Salient and tombolo geometry and shape. *Journal of Coastal Research*, *SI*(29), 82–93.

Black, K., & Mead, S. (2001). Design of the Gold coast reef for surfing, public amenity and coastal protection: Surfing aspects. *Journal of Coastal Research*, *SI*(29), 115–130.

Buckley, M. L., Lowe, R. J., Hansen, J. E., & Van Dongeren, A. R. (2015). Dynamics of wave setup over a steeply sloping fringing reef. *Journal of Physical Oceanography*, *45*(12), 3005–3023. https://doi.org/10.1175/JPO-D-15-0067.1

Buckley, M. L., Lowe, R. J., Hansen, J. E., & Van Dongeren, A. R. (2016). Wave setup over a fringing reef with large bottom roughness. *Journal of Physical Oceanography*, *46*(8), 2317–2333. https://doi.org/10.1175/JPO-D-15-0148.1

da Silva, R. F., Hansen, J. E., Rijnsdorp, D. P., Lowe, R. J., & Buckley, M. L. (2022). The influence of submerged coastal structures on nearshore flows and wave runup. *Coastal Engineering*, *177*, 104194. https://doi.org/10.1016/j.coastaleng.2022.104194

da Silva, R. F., Rijnsdorp, D. P., Hansen, J. E., Lowe, R., Buckley, M., & Zijlema, M. (2021). An efficient method to calculate depth-integrated, phase-averaged momentum balances in non-hydrostatic models. *Ocean Modelling*, *165*, 101846. https://doi.org/10.1016/j.ocemod.2021.101846

da Silva, R. F., Storlazzi, C. D., Rogers, J. S., Reyns, J., & McCall, R. (2020). Modelling three-dimensional flow over spur-and-groove morphology. *Coral Reefs*, *39*(6), 1841–1858. https://doi.org/10.1007/s00338-020-02011-8

Dean, R. G., Chen, R., & Browder, A. E. (1997). Full scale monitoring study of a submerged breakwater, Palm Beach, Florida, USA. *Coastal Engineering*, *29*(3–4), 291–315. https://doi.org/10.1016/S0378-3839(96)00028-2

Duarte Nemes, D., Fabián Criado-Sudau, F., & Nicolás Gallo, M. (2019). Beach morphodynamic response to a submerged reef. *Water*, *11*(2), 340. https://doi.org/10.3390/w11020340

Falter, J. L., Lowe, R. J., Zhang, Z., & McCulloch, M. (2013). Physical and biological controls on the carbonate chemistry of coral reef waters: Effects of metabolism, wave forcing, sea level, and geomorphology. *PLoS One*, *8*(1), e53303. https://doi.org/10.1371/JOURNAL.PONE.0053303

Feddersen, F., Clark, D. B., & Guza, R. T. (2011). Modeling surf zone tracer plumes: 1. Waves, mean currents, and low-frequency eddies. *Journal of Geophysical Research*, *116*, C11027. https://doi.org/10.1029/2011JC007210

Feddersen, F., Guza, R. T., Elgar, S., & Herbers, T. H. C. (1998). Alongshore momentum balances in the nearshore. *Journal of Geophysical Research*, *103*(C8), 15667–15676. https://doi.org/10.1029/98JC01270

Haller, M. C., Dalrymple, R. A., & Svendsen, I. A. (2002). Experimental study of nearshore dynamics on a barred beach with rip channels. *Journal of Geophysical Research*, *107*(C6), 3061. https://doi.org/10.1029/2001JC000955

Hansen, J. E., Elias, E., List, J. H., Erikson, L. H., & Barnard, P. L. (2013). Tidally influenced alongshore circulation at an inlet-adjacent shoreline. *Continental Shelf Research*, *56*, 26–38. https://doi.org/10.1016/j.csr.2013.01.017

Hansen, J. E., Janssen, T. T., Raubenheimer, B., Shi, F., Barnard, P. L., & Jones, I. S. (2014). Observations of surfzone alongshore pressure gradients onshore of an ebb-tidal delta. *Coastal Engineering*, *91*, 251–260. https://doi.org/10.1016/j.coastaleng.2014.05.010

Hansen, J. E., Raubenheimer, B., List, J. H., & Elgar, S. (2015). Modeled alongshore circulation and force balances onshore of a submarine canyon. *Journal of Geophysical Research: Oceans*, *120*, 1887–1903. https://doi.org/10.1002/2014JC010555

Long, J. W., & Özkan-Haller, H. T. (2005). Offshore controls on nearshore rip currents. *Journal of Geophysical Research*, *110*, C12007. https://doi.org/10.1029/2005JC003018

Longuet-Higgins, M. S., & Stewart, R. w. (1964). Radiation stresses in water waves; a physical discussion, with applications. *Deep Sea Research and Oceanographic Abstracts*, *11*(4), 529–562. https://doi.org/10.1016/0011-7471(64)90001-4

Lowe, R. J., Falter, J. L., Bandet, M. D., Pawlak, G., Atkinson, M. J., Monismith, S. G., & Koseff, J. R. (2005). Spectral wave dissipation over a barrier reef. *Journal of Geophysical Research*, *110*, C04001. https://doi.org/10.1029/2004JC002711

Lowe, R. J., Falter, J. L., Monismith, S. G., Atkinson, M. J., Lowe, R. J., Falter, J. L., et al. (2009). Wave-driven circulation of a coastal reef–Lagoon system. *Journal of Physical Oceanography*, *39*(4), 873–893. https://doi.org/10.1175/2008JPO3958.1

Mei, C. C., Stiassnie, M., & Yue, D. K.-P. (2005). *Theory and applications of ocean surface waves*. World Scientific. https://doi.org/10.1142/5566

Monismith, S. G. (2007). Hydrodynamics of coral reefs. *Annual Review of Fluid Mechanics*, *39*(1), 37–55. https://doi.org/10.1146/annurev.fluid.38.050304.092125

Moulton, M., Elgar, S., Raubenheimer, B., Warner, J. C., & Kumar, N. (2017). Rip currents and alongshore flows in single channels dredged in the surf zone. *Journal of Geophysical Research: Oceans*, *122*, 3799–3816. https://doi.org/10.1002/2016JC012222

Mulligan, R. P., Hay, A. E., & Bowen, A. J. (2010). A wave-driven jet over a rocky shoal. *Journal of Geophysical Research*, *115*, 10038. https://doi.org/10.1029/2009JC006027

Poate, T., Masselink, G., Austin, M. J., Inch, K., Dickson, M., & McCall, R. (2020). Infragravity wave generation on shore platforms: Bound long wave versus breakpoint forcing. *Geomorphology*, *350*, 106880. https://doi.org/10.1016/j.geomorph.2019.106880

Pondella, D. J., II, Jonathan, W., Jeremy, C., Becky, S., Kerry, R., & Ken, S. (2015). The physical characteristics of nearshore rocky reefs in the southern California Bight. *Bulletin Southern California Academy of Sciences*, *114*(3), 105–122. https://doi.org/10.3160/soca-114-03-105-122.1

Quataert, E., Storlazzi, C., van Rooijen, A., Cheriton, O., & van Dongeren, A. (2015). The influence of coral reefs and climate change on wave-driven flooding of tropical coastlines. *Geophysical Research Letters*, *42*, 6407–6415. https://doi.org/10.1002/2015GL064861

Ranasinghe, R., Larson, M., & Savioli, J. (2010). Shoreline response to a single shore-parallel submerged breakwater. *Coastal Engineering*, *57*(11–12), 1006–1017. https://doi.org/10.1016/j.coastaleng.2010.06.002

Ranasinghe, R., Turner, I. L., & Symonds, G. (2006). Shoreline response to multi-functional artificial surfing reefs: A numerical and physical modelling study. *Coastal Engineering*, *53*(7), 589–611. https://doi.org/10.1016/j.coastaleng.2005.12.004

Raubenheimer, B., Guza, R. T., & Elgar, S. (2001). Field observations of wave-driven setdown and setup. *Journal of Geophysical Research*, *106*(C3), 4629–4638. https://doi.org/10.1029/2000JC000572

Rijnsdorp, D. P., Buckley, M. L., da Silva, R. F., Cuttler, M. V. W., Hansen, J. E., Lowe, R. J., et al. (2021). A numerical study of wave-driven mean flows and setup dynamics at a coral reef-Lagoon system. *Journal of Geophysical Research: Oceans*, *126*, e2020JC016811. https://doi.org/10.1029/2020JC016811

Rijnsdorp, D. P., Ruessink, G., & Zijlema, M. (2015). Infragravity-wave dynamics in a barred coastal region, a numerical study. *Journal of Geophysical Research: Oceans*, *120*, 4068–4089. https://doi.org/10.1002/2014JC010450

Rosman, J. H., & Hench, J. L. (2011). A framework for understanding drag parameterizations for coral reefs. *Journal of Geophysical Research*, *116*, C08025. https://doi.org/10.1029/2010JC006892

Segura, L. E., Hansen, J. E., & Lowe, R. J. (2018). Seasonal shoreline variability induced by subtidal water level fluctuations at reef-Fringed beaches. *Journal of Geophysical Research: Earth Surface*, *123*, 443–447. https://doi.org/10.1002/2017JF004385

Smit, P., Janssen, T., Holthuijsen, L., & Smith, J. (2014). Non-hydrostatic modeling of surf zone wave dynamics. *Coastal Engineering*, *83*, 36–48. https://doi.org/10.1016/j.coastaleng.2013.09.005

Smit, P., Zijlema, M., & Stelling, G. (2013). Depth-induced wave breaking in a non-hydrostatic, near-shore wave model. *Coastal Engineering*, *76*, 1–16. https://doi.org/10.1016/j.coastaleng.2013.01.008

Sous, D., Dodet, G., Bouchette, F., & Tissier, M. (2020). Momentum balance across a barrier reef. *Journal of Geophysical Research: Oceans*, *125*, e2019JC015503. https://doi.org/10.1029/2019JC015503

Suh, K., & Dalrymple, R. A. (1987). Offshore breakwaters in laboratory and field. *Journal of Waterway, Port, Coastal, and Ocean Engineering*, *113*(2), 105–121. https://doi.org/10.1061/(ASCE)0733-950X(1987)113:2(105)

Villani, M., Bosboom, J., Zijlema, M., & Stive, M. J. (2012). Circulation patterns and shoreline response induced by submerged breakwaters. *Coastal Engineering Proceedings*, *1*(33), 25. https://doi.org/10.9753/icce.v33.structures.25

Winter, G., Lowe, R. J., Symonds, G., Hansen, J. E., & van Dongeren, A. R. (2017). Standing infragravity waves over an alongshore irregular rocky bathymetry. *Journal of Geophysical Research: Oceans*, *122*, 4868–4885. https://doi.org/10.1002/2016JC012242

Zijlema, M., & Stelling, G. S. (2005). Further experiences with computing non-hydrostatic free-surface flows involving water waves. *International Journal for Numerical Methods in Fluids*, *48*(2), 169–197. https://doi.org/10.1002/fld.821

Zijlema, M., & Stelling, G. S. (2008). Efficient computation of surf zone waves using the nonlinear shallow water equations with non-hydrostatic pressure. *Coastal Engineering*, *55*(10), 780–790. https://doi.org/10.1016/j.coastaleng.2008.02.020

Zijlema, M., Stelling, G., & Smit, P. (2011). Swash: An operational public domain code for simulating wave fields and rapidly varied flows in coastal waters. *Coastal Engineering*, *58*(10), 992–1012. https://doi.org/10.1016/j.coastaleng.2011.05.015